Single Crystalline 100% epi-Ge Layers on Engineered Oxide Heterostructures on Si

Peter Rodenbach

Oktober 2008

Diplomarbeit

Fachbereich Physik der

Freien Universität Berlin

Betreuer: Prof. Dr. J.-I. Pascual

This thesis was carried out in collaboration of AG J.I. Pascual at Freie Universität Berlin and the AG T. Schroeder at the Leibniz Institute IHP - innovations for high performance microelectronics in Frankfurt (Oder).

Berlin, October 2008.

"Alles prüfe der Mensch, sagen die Himmlischen,
Daß er, kräftig genährt, danken für Alles lern’,
Und verstehe die Freiheit,
Aufzubrechen, wohin er will."

aus Friederich Hölderlins "Lebenslauf".

Abstract

Single crystalline Germanium (Ge) has gained a lot of attention for applications as new material in microelectronics, photovoltaics and for photodetectors. The integration on the mature and predominating Silicon (Si) technology platform is a challenging technical task, which offers many basic scientific questions to be answered.

This thesis is concerned with the integration of a functional Ge layer on the Si platform via an engineered oxide heterostructure, namely cubic PrO_2. The oxide is incorporated to compensate for the 4% lattice constant mismatch of Ge and Si, with its lattice constant between the two semiconductors. An in situ reflection high energy electron diffraction (RHEED) monitoring of the layer deposition by molecular beam epitaxy (MBE) indicates that the initial growth mode of Ge on PrO_2 follows a Volmer-Weber growth mode due to interface reactions, surface and strain energies. By properly tuning the growth parameters of MBE a growth recipe is developed, leading to the growth of atomically smooth single crystalline Ge (111) layers on the Pr_2O_3 (111) / Si (111) support system. The oxide is subject to a chemical reduction process during the Ge deposition, resulting in a Pr_2O_3 stoichiometry. The closed layers are not achieved by a change to van der Merwe growth, but by the adjustment of the growth kinetics, resulting in a smoothing out of the Volmer-Weber growth (Fig. 1). The development of the recipe for the Ge layer growth is monitored with RHEED, ex situ x-ray reflectivity (XRR) and x-ray diffraction (XRD) measurements as well as scanning electron microscopy (SEM). These methods confirm the closed and smooth Ge surface and the sharp interface with the underlying Pr_2O_3. The closed layer stacks are investigated by synchrotron radiation x-ray diffraction under bulk sensitive and surface sensitive measurement conditions. This first study unveils a single crystalline type A / B / A stacking configuration of the Ge (111) / Pr_2O_3 (111) / Si (111) heterostack system.

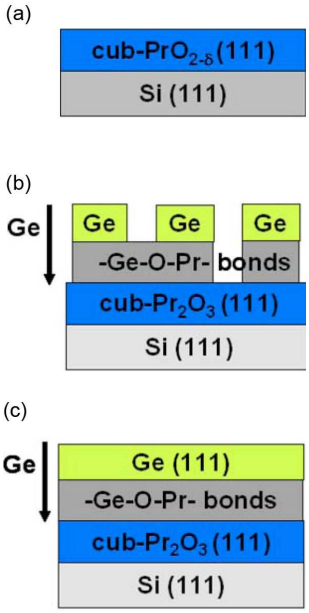

FIG. 1: The development of the Ge layer growth with deposition time. From the initial Volmer-Weber growth to the final smooth layer.

Driven by the results from the structural investigation a second study reveals the main defect mechanisms at work by XRD pole-figure measurements and reciprocal space maps (RSMs), supported by real space cross section transmission electron microscopy (TEM) images along a stacking sensitive direction. The defects limiting the long range order in the Ge layer are identified as stacking twins, microtwins and stacking faults (Fig. 2). The investigation of the thickness dependent behaviour discloses a threading behaviour of microtwins and stacking faults while stacking twins are confined to the interface. First results of high temperature UHV annealing experiments show the reduction of diffuse scattering by strain fields in defective Ge is possible, indicating a reduction of stacking faults, while microtwins as well as stacking twins are not influenced by the annealings. Future defect engineering approaches are required to improve the long range order of the epi-Ge layer for technological applications.

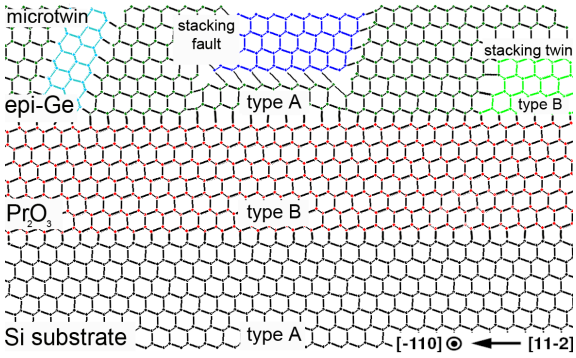

FIG. 2: Epitaxial relationship and main defect mechanisms at work in the epi-Ge layer.

Zusammenfassung

Einkristallines Germanium (Ge) erfreut sich erneuter Aufmerksamkeit für die Anwendung in der Mikroelektronik, in der Photovoltaik und in Photodetektoren. Die Integration von Germanium auf der weit entwickelten und verbreiteten Silizium (Si) Technologieplattform ist eine Herausforderung, im Zuge derer viele interessante zu Grunde liegende wissenschaftiche Fragen beantwortet werden können. Die vorliegende Arbeit befasst sich mit der Integration einer funktionalen Ge Schicht auf der Si Technologieplattform mit Hilfe einer flexibel adaptierbaren Oxyd-Heterostruktur. Das Oxyd, kubisches PrO_2, wird zwischen Ge und Si eingebaut, um den Stress zu kompensieren, der durch den 4% Unterschied der Gitterkonstanten von Si und Ge hervorgerufen wird. Die während der Deposition aufgenommenen Beugungsbilder hochenergetischer Elektronen in Reflexionsgeometrie (RHEED) zeigen, dass Ge aufgrund von Oberflächenenergien und der Grenzflächenwechselwirkung in einem Volmer-Weber Wachstumsmodus aufwächst. Im Zuge dieser Arbeit wurde dennoch, über die Anpassung der Wachstumsbedingungen (d.h. Ge Fluss und Substrattemperatur) in der Molekularstrahlepitaxie (MBE), ein Wachstumsrezept entwickelt, welches das Wachstum von flachen, einkristallinen Ge Schichten auf dem Si (111) / Pr_2O_3 (111) System ermöglicht. Die geschlossenen Ge Filme werden nicht über einen Wechsel des Wachstumsmodus hin zu einem Frank - van der Merwe Modus erreicht, sondern über eine Anpassung der Wachstumskinetik, die ein Ausglätten der Ge Schichten zur Folge hat, wie im Piktogramm (Fig. 1) gezeigt. Die Weiterentwicklung des Wachstumsrezepts wurde mit in-situ RHEED, ex-situ Röntgenreflektometrie (XRR) und Röntgenbeugung (XRD) sowie Rasterelektronenmikroskopie (SEM) überwacht. Diese Messungen bestätigen die geschlossene glatte Oberfläche der Ge Schichten, sowie die Schärfe der Ge / Pr_2O_3 Grenzfläche. Die geschlossenen Schichtsysteme sind des weiteren mit Synchrotronstrahlung XRD unter volumen- und oberflächensensitiven Messbedingungen untersucht worden. Diese erste Studie zur Epitaxie und Kristallinität enthüllt eine einkristalline Typ A / B / A Epitaxie des Ge (111) / Si (111) / Pr_2O_3 (111) Systems.

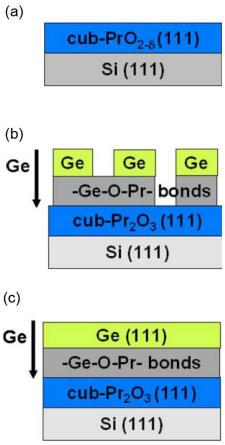

FIG. 1: Ge Schichtwachstum: Von Volmer- Weber Inseln zu geschlossenen Schichten.

Motiviert durch die Ergebnisse der Röntgenbeugungsuntersuchungen zeigt der zweite Teil der Studie die wichtigsten Defektmechanismen auf, die die langreichweitige Ordnung in den Ge Schichten stören. Die hierbei verwendeten Methoden sind XRD-Polfiguren, Karten des reziproken Raums in der Nähe von Bragg-Reflexen (RSMs) sowie Querschnitts-Transmissionselektronenmikroskopie (TEM) Bilder. Die Defekte können als Stapelfehler, Stapelzwillinge sowie Mikro-Zwillinge identifiziert und quantifiziert werden, wie schematisch in Fig. 2 zusammengefasst. Eine Untersuchung der Schichtdickenabhängigkeit der Defekte zeigt, dass Stapelzwillinge auf den grenzflächennahen Bereich zum Oxyd hin beschränkt sind, wohingegen Stapelfehler und Mikro-Zwillinge die gesamte Ge Schicht durchziehen. Erste Ergebnisse von Temperversuchen an dem Schichtsystem im Ultrahochvakuum deuten darauf hin, dass sich Stapelfehler hierdurch verringern lassen, Stapelzwillinge und Mikro-Zwillinge hingegen jedoch nicht. Um eine Einführung in die Technologie voranzutreiben, wird in Zukunft eine darüber hinausgehende Beeinflussung der Defektdichten zur Vergrösserung der langreichweitigen Ordnung in den Ge Schichten vonnöten sein.

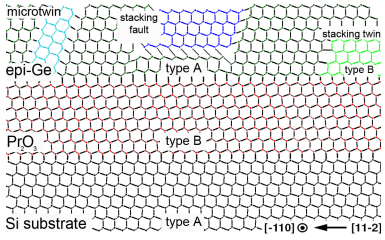

FIG. 2: Die wichtigsten Defektmechanismen im epitaktischen Germanium.

Contents

1 Motivation

1.1 Engineered Si Wafer

The concept of the integration of single crystalline 100% epitaxial (epi)-Germanium (Ge) layers on Silicon (Si) (111) via an engineered oxide heterostructure belongs to the strategy of so-called "engineered wafer" systems. Fig. 1 shows such a system, and that it consists of a Si wafer substrate, a buffer layer, and a functional semiconductor layer. An engineered wafer is therefore generally defined as: the combination of different semiconductor material layers that lead to a unique final product that cannot be built on silicon alone. It has to be noted that an engineered wafer most commonly uses Si as the material platform. The manufacturing techniques of Si have, along with the development of microelectronics, undergone 60 years of research, and thus have reached a high level of perfection, in terms of defect density, purity, diameter, technology, etc. The vision of such an engineered wafer is described by the following six

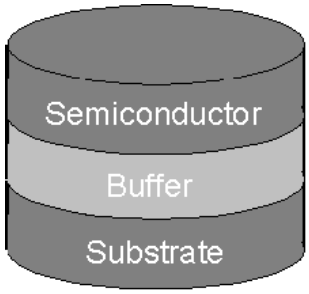

FIG. 1: Engineered Wafer System

criteria:

1. The integrated materials system is an active circuit element:
   Example: GaAs (Gallium-Arsenide) on Si to combine the favourable III-V applications (optoelectronics) with the predominating Si applications (digital data processing).

2. The integrated materials system serves as a buffer:
   Example: GaAs on Si serves as a buffer layer for GaInP (Gallium Indium Phosphite) for photovoltaics.

3. The exploitation of the mature Si wafer technology:
   Example: Handling and production of Si wafers have been perfected and established for large substrates with 300 mm diameter.

4. The optimal combination of favourable thermal and mechanical properties:
   Example: 100% GaAs wafers are very brittle and require more careful treatment than Si wafers.

5. The design of thin film properties that differ from the bulk properties of the same material:
   Example: Strained Si layers show a higher charge carrier mobility than bulk Si.

6. Providing semiconductor substrates that do not yet exist:
   Example: There are no GaN (Gallium-Nitride) bulk substrates of sufficient quality.

Summarized, the successful engineering of wafers will allow higher device functionality and performance on a well established substrate technology at low cost [1]. However, it has to be stressed that the integration of functional semiconductors on the Si technology platform via an engineered wafer system is only one important approach among others. Besides the global integration of the new material onto the entire Si substrate, the deposition of the functional layer can in principle also be limited locally to the area of a future device.
The assets und drawbacks of global and local integration have to be carefully balanced to reach the most favourable, i.e., the cost-effective solution.

1.2 Applications

The realization of single crystalline 100% epi-Ge layers of high quality on the Si material platform would have the most powerful impact on the following areas:

1.2.1 Highly Integrated Microelectronics

In highly integrated microelectronics, Ge was initially the first material investigated as transistor material. In 1947, the first transistor was created at Bell Laboratories by William Shockley, John Bardeen and Walter Brattain, who received the Nobel Price in 1956 for the research associated with this invention. As the first model, the following commercial transistors were manufactured of Ge, which correspondingly became the model for understanding semiconductor physics. In 2000, Jack S. Kilby received the Nobel Price for his contributions to the invention of the integrated circuit, in which again Ge had been used as the transistor material at first. At the beginning of the 1950's Ge appeared to be the most promising semiconductor, as its purification was considerably easy due to its low melting point at 937°C and low vapour preassure at the melting point. Nevertheless, Ge was to be replaced by Silicon (001) in 1955[1], which subsequently became the predominating material in microelectronics, as the higher band gap of Si (1.1 eV) allowed for higher temperature device operations than Ge based transistors. The improvement of Si purification techniques allowed this transition. In addition, the stable Si dioxide showed, in contrast to the unstable native Ge oxide, high thermal stability, a good semiconductor-oxide interface, and good microprocessing as well as electrical properties [2].

[1] The transition from Ge to Si did not occur on a definite date. It was rather a slow, but steady transition process, in which the favourable properties of Si became more and more evident. As the first planar Si transistor was built in 1955 by Jean Hoerni, this date is given as reference [2].

The increase in performance up to nowadays can be attributed to the 'scaling' process, viz the reduction of device dimensions which results in the higher number of features per square unit of Si, following Moore's law that predicts a doubling of transistors per square unit every 24 months [3]. The development over the last decades can be seen in Fig. 2 [4]. This 'law' is part of the International Technology Roadmap for Semiconductors (ITRS) and thereby business objective for all Integrated Circuit Manufacturers (ICMs). The reduction in size has led to a transistor gate width of 45 nm in production today. As the gate width is reduced, the dielectric layer thickness decreases as well, leading to only 8 Å of Si dioxide. At this thickness, the oxide loses its mandatory insulating properties, resulting in an intolerable leakage current density at further scaling. Thus the process of miniaturization has reached its physical boundaries for the used material system.

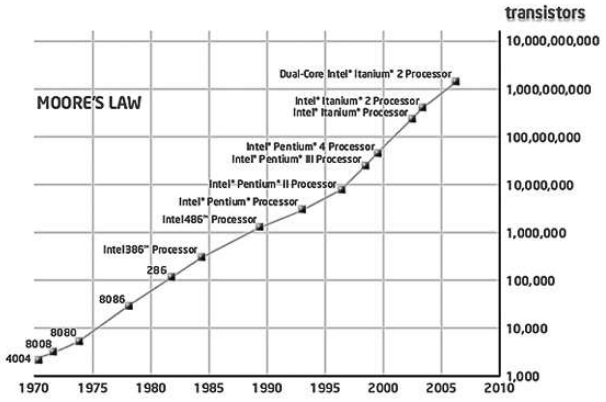

FIG. 2: Development of transistors per chip

The basic idea of a Metal Oxide Semiconductor Field Effect Transistor (MOSFET), consisting of source, drain, gate, and substrate contacts (see Fig. 3), is to modulate the resistance in the channel between source and drain. By applying a voltage between base and gate, the resistance of the channel is modified. The voltage at the gate induces charges on the other side of the insulator (the oxide) in the semiconductor, thereby creating the conducting channel that connects source and drain electrode. If the oxide does not insulate gate and semiconductor channel due to insufficient thickness, the transistor is not switchable anymore. For a comprehensive understanding of different transistor architechtures see [5]. In addition, ICMs face exploding tool costs, which is described by Rock's law, according to which the prices for tools used in the fabrication process of chips double every 48 months. Albeit the ICM's reluctance towards integrating new materials into the mainstream Si transistor technologies these recent devolpments demand new approaches in order to secure further development in highly integrated microelectronics. There are several different ideas of how to pursue further advance that can be summarized under the key notes "More of Moore" and "More than Moore". "More of Moore" refers to the further device miniaturisation on the Si platform, but using different strategies. "More than Moore" refers to strategies and processes other than the scaling process. Some examples for the above mentioned are:

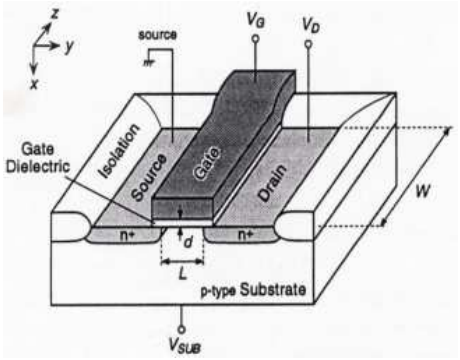

FIG. 3: Planar MOSFET architecture

– "More of Moore":
  3D Transistors (3D FinFET(Fin-Field Effect Transistors)), more than two gate transistors and Si nanowire transistors with all-around gate electrodes, etc.

- "More than Moore":
  The global integration of strained Si layers, the local integration of high-k dielectrics, which Intel has implemented by Hafnium based oxide and announced that the production would start throughout 2008. The integration of Ge and III-V semivonductors as high mobility channel materials are currently under intensive research.

As the latter point is of special interest to this thesis, it will be elaborated on further. Ge as semiconductor material is of such interest to the integration in Complementary Metal Oxide Semiconductors (CMOS) for the following reasons [6]:

- Same crystal lattice structure as Si, i.e., the diamond lattice, with 4% lattice constant mismatch
- Smaller band gap than Si of 0.66 eV
- The electron mobility is 2.6 times higher than for Si
  The hole mobility is 4.6 times higher than for Si
- The higher density of states in the conduction band allows higher drive currents than all other III-V semiconductors
- Low dopant activation energy
- Similar electron affinity compared to Si

1.2.2 Photodetectors and Optoelectronics

As the combination of electronics and photonics becomes more and more important, there is a need for the combination of both functionalities. A well known example are the common so called Charge Coupled Devices (CCD), combined with CMOS, in digital cameras.
Again, Si is up to now the predominant material in use. Nevertheless, Si has the disadvantage that its high indirect band gap prevents sufficient light detection in the standardized frequency bands of telecommunications. The maximum detectable wavelength for Si detectors is 850 nm. Ge, on the contrary, exhibits a higher absorbtion coefficient (α) in this frequency range, and is used for optical communications applications for near infrared wavelengths ($\alpha_{Ge} \approx 10^3 \alpha_{Si}$), which are the preferred wavelengths for fiber optical systems. Again Ge is advantageous for the utilization in photodetectors as it is compatible with the Si technology platform with a high cost efficiency [7]. Si also suffers, in this range, from severe self absorption in waveguides. Both Si and Ge are indirect semiconductors, and therefore have a poor absorption directly above the band gap, but the absorption curve of Ge is much steeper for energies slightly above the band gap. This is caused by the short energetic distance to the first direct transition, which is slightly above the indirect transition (0.2 eV). For Si the next direct transition is far above the indirect one (1.12 eV). Furthermore, an isolated Ge film prevents the collection of slow carriers generated by

the substrate. Summarized the absorption is 50 times larger for Ge than for Si for the visible and NIR (Near Infra Red) range, and several orders of magnitude for lower energies (850 nm – 1500 nm). The above mentioned higher charge mobilities in Ge allow short detector transit times: For this example, a high speed operation at 850 nm has been demonstrated [8]. Some groups have reported a Ge detector operation at 40 GHz, even operation beyond 100 GHz is proposed [9].

1.2.3 Photovoltaics

The global deposition of Ge over the entire Si substrate wafer is of special interest for photovoltaics. The highest energy conversion rate for a solar cell has been realized with multiple junction solar cells, reaching between 30% and 50%. The energy conversion rate (η) is defined as:

$$\eta = \frac{P_m}{E \cdot A_c}$$

where P_m is the maximum power generated by the cell, E the irradiance, and A_c the size of the cell. A multiple junction cell consists of multiple thin layers of different semiconductors. This setup is chosen because the different bandgap of the semiconductors allow a broader absorption and conversion of the solar radiation spectrum. Single junction Si based cells cannot utilize the infrared part of the solar spectrum as the band gap of Si amounts to 1.1 eV. Compared to the multiple junction cells, the highest conversion rates of conventional amorphous Si cells are around 19%, of Cadmium Telluride (CdTe) cells around 18% and of Copper Indium Gallium Selenide (CIGS) around 19.5%, which are obviously much smaller. One of the most efficient setups in production is a Triple Junction cell, consisting of Ge as a substrate and GaInP on top of GaAs as epi layers, which are grown by metal-organic chemical vapour deposition [10]. Ge is used as a substrate owing to the fact that GaAs can be grown directly epitaxally on top, since the materials have a lattice mismatch of only 0.004 Å (d_{GaAs}=5.6535Å, d_{Ge}=5.6577Å [11]). In principle, the fabrication of Ge wafers is possible, since the generation of dislocations in the bulk crystal is thermodynamically not stable, because they enlarge Gibb's Free Energy [12]. The state-of-the-art production of Ge substrate wafers are produced by the Belgium based Umicore EOM company using the Czochralski (CZ) pulling technique in the size of 4"[13]. The CZ technique is a crystal growth method, where a single crystal is pulled from a melt using a small single crystalline seed, whose orientation and structure is adopted by the growing crystal. Even 12" wafers have been manufactured, but not yet in commercially usable quality. Due to the high price of the Ge wafers, the total price of such photovoltaic panels consists of about 40% of the substrate material, thereby reserving this Triple Junction cells exclusively to space applications, where they present the predominant solar cell setup [14]. Some terrestrial applications have been taken into consideration in so-called concentrator photovoltaic systems, where large mirrors and lenses focus the sun light on a small Triple Junction cell, but a commercial breakthrough is yet to be observed.

By providing large, high quality epi-Ge layers in a cost-effective way on the comparatively cheap Si

wafer platform, and thereby lowering the Ge substrate costs for GaAs photovoltaics, an impediment to high performance GaAs solar cell technology entering the mass market of terrestrial applications, would be removed.

1.3 Engineered Wafer Preparation

1.3.1 Layer Transfer

The currently established and most feasible technology for the combination of different semiconductor material layers with Si is the so-called Smart Cut™ (henceforth Smart Cut) layer-transfer technology [15], which allows two bulk material wafers to be combined. The Smart Cut process begins with the formation of a dielectric oxide layer on the wafers. After this, a Hydrogen implant through the oxidized surface creates a line of defects at a certain depth corresponding to the implantation depth of the Hydrogen implant. This oxidized wafer is then bonded to another substrate wafer and annealed. During the annealing process, the defects coalesce into cavities, splitting the top layers off, creating a thin layer of the new material on the oxide of the substrate wafer, as exemplarily shown for a 'Germanium-on-Insulator' (GoI) layer on a Si substrate in Fig. 4. After the transfer, both surfaces are very rough. Only after polishing and chemical treatment the surface becomes smooth. This technique basically allows the realization of the vision 'anything on anything', but as reported by the manufacturing companies, the quality for a Ge layer on Si dioxide, attained in the Smart Cut process is up to now quite poor, containing a too high dislocation density in the Ge layer [8, 16].

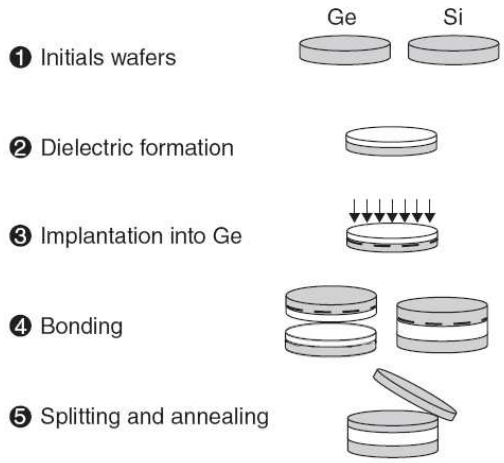

FIG. 4: Smart Cut Process [12]

1.3.2 Heteroepitaxy

The effort to integrate Ge in Si mainstream technologies was already made during the 1990's, leading to a material that became predominat for niche applications in mixed signal / high frequency microelectronics. The successfully produced material is the so called Silicon-Germanium (SiGe), in which Si and Ge are grown heteroepitaxially as an alloy directly on the Si wafer in order to engineer the band offsets. To compensate the strain, the Si content is gradually reduced with increasing thickness. A final ratio of $x = 0.2$ for $Si_{1-x}Ge_x$ is nowadays realized in high quality layers with a high reliability, so that these layers are of technological and commercial relevance. The technological impact of this materials system is surprisingly high in the field of SiGe-Bipolar transistor technology for high power / high frequency applications. The compatibility with the Si platform allowed to join SiGe-Bipolar with Si CMOS,

which is exploited in form of SiGe-Bi-CMOS technologies for wireless communications systems at the present day [17]. The IHP in Frankfurt (Oder), with its cleanroom pilot line manufacturing 130 nm SiGe Bi-CMOS technologies, is among the world leaders in this research and development field.

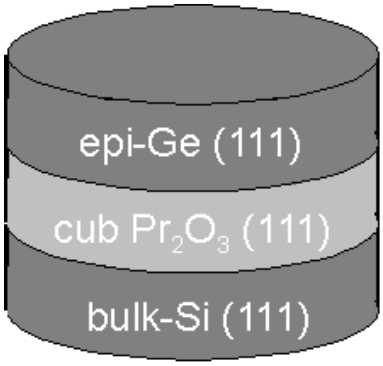

FIG. 5: The IHP Approach [18]

Following the same strategy, an implementation of 100% Ge layers via a graded SiGe buffer has been undertaken, but failed in the terms of layer quality for ratios above the mentioned 20% Ge. In this context of the classical heteroepitaxial integration of the high quality Ge layer on Si (111), the implementation via an engineered oxide heterostructure is a completely new approach, as chosen by the "Heteroepitaxy" research project at the Leibniz Institue IHP [18] to which this thesis contributed. The system in our project consists of Si (111) wafers, and a thin Praseodymium oxide buffer (Pr_2O_3, PrO_2) layer on which Ge is deposited. Both epi-layers are either deposited by Molecular Beam Epitaxy (MBE) or Chemical Vapour Deposition (CVD). The oxide is incorporated between the Si and Ge to compensate the strain caused by the 4% lattice mismatch between the two semiconductors. As the Ge on the oxide layer is deposited globally on the entire surface of the Si wafer, and the chosen wafer orientation of the [111] direction, this project, in principle, has the goal to provide suit Ge substrates for the photovoltaic technology branch.

Pr oxide was chosen primarily for its lattice constant ($a = \frac{1}{2} \cdot 11.152$ Å) that is about 2.4% bigger than the one of Si ($a = 5.4305$ Å) and about 1.6% smaller than the one of Ge ($a = 5.65675$ Å), thereby posing a reasonable mediator between the two semiconductors. Furthermore, Pr oxide has a cubic bixbyite configuration in which the Pr sublattice shows a high thermal stability up to 700°C, allowing for high temperature processing steps without the risk of metal contamination in the semiconductor layer. The advantage of this approach is that it is very flexible in terms of the used materials and the integrated semiconductor, as well as the availability of the technology, which is present at most semiconductor manufacturing sites as some of the processing steps are applied in CVD reactors.

At the time this thesis started, the previously gained scientific results in the running Heteroepitaxy project were:

- The deposition of single crystalline Pr_2O_3 on Si (111) was accomplished, and the epitaxial behaviour investigated [19].
- The deposition of single crystalline self-assembled Ge nanocrystals on cubic Pr_2O_3 on Si(111) was realized [20].
- Single crystalline PrO_2 was successfully prepared by ex-situ oxygen annealing of the as deposited Pr oxide on Si(111) [21].
- The initial growth mechanism and interface reactions during deposition of Ge on the PrO_2 / Si (111) support system had been thoroughly studied [22].

1.4 Defects

Due to the vast amount of variables in crystal growth and the challenge of manipulations on the atomic scale no crystal can be grown without the incorporation of defects. Defects are characterized as point, line and surface defects, dependent on their dimension. The presence of defects is strongly contributing to the macroscopic behaviour of a material and is not necessarily a drawback, as implied by the denotation. Some important examples are: The current fabrication of steel would be impossible without the understanding of the incorporation of carbon atoms. In general the combination of small amounts of other metals to alloys is enabling lightweight constructions with superior flexibility and mechanical strength compared to pure metals. In microelectronics the transistor would not work without the implantation of n- or p-type donor atoms (point defects) in the otherwise almost perfect Si matrix. The intentional incorporation of internal material stresses by dislocations is a new area of research for high mobility conductors. In photovoltaics the amount of grain boundaries, as recombination centers for electrons and holes, is very important for the performance of each cell.
The identification and understanding of defects in Ge is thus inevitable in material science to influence the mechanical, electrical and thermal behaviour of the studied material in general.

1.5 Aim of the Diploma Thesis

At the starting point of this thesis, the far too high surface roughness and defect density of the Ge layer posed, however, a major obstacle that renders any of the above mentioned applications impracticable. As the interaction physics of Ge and the Pr oxides, namely the formation of defects and wetting behaviour, as well as their engineering, have scarcely been studied, this became the authors task in the heteroepitaxy project at IHP and is therefore the central theme of this thesis. The main assignments of the diploma-project were the following two topics:

1. **Structure:**
   The study of the structure and surface behaviour of the epi-Ge layer, and the preparation of smooth, closed epi-layers by adjustment of the growth conditions (mainly flux and temperature); the investigation of the influence of growth parameters, especially the ones of flux and temperature, on the wetting behaviour of the Ge deposits on the Pr oxide / Si(111) support system.

2. **Defects:**
   As epitaxial growth is impossible without crystalline defects, the identification and study of grown-in defects in the material system, and likewise the determination of the influence of the growth parameters on the defects in terms of types, distribution and threading behaviour.

The most important methods used and discussed are ex-situ laboratory and synchrotron based X-Ray Reflectivity (XRR), X-Ray Diffraction (XRD) and in-situ growth monitoring by Reflection High Energy

Electron Diffraction (RHEED). Additional information on defects is provided by Transmission Electron Microscopy (TEM) and Scanning Electron Microscopy (SEM).

1.6 Organisation of the Thesis

The work entailed with this thesis is concerned with the growth and improvement of epi-Ge layers. It strictly follows the order of the preparation- and investigation-procedure of each sample: from initial Si wafer preparation to the final characterization by various techniques.

Chapter 2 gives a short overview on the theoretical and experimental principles applied in this study. For the sake of the extent of this thesis, each method or procedure is briefly reviewed, with reference to the standard literature on each topic that allows a broad and more comprehensive understanding.

Chapter 3 states the results and a discussion, for the information obtained in the carried out experiments, and for both the preparation of closed smooth Ge samples (structure) as well as the study on defects in the Ge layers.

Chapter 4 summarizes the results and gives a short evaluation of the work of this study in terms of the implications given by the obtained results and states some recommendations for future efforts.

2 Experimental Background

2.1 Substrates for Film Deposition

The used substrates are single crystalline Si wafers, provided by the company Siltronic. They have a diameter of 4" (100 mm) and are 525 ± 15 μm thick. The wafers are produced by Czochralski pulling. The used surface orientation is the [111] $\pm$ (0.5°) direction. The miscut of 0.5° is in the [1$\bar{1}$0] direction, which is indicated by the wafer flat. The doping is of the p type, the dopant is Bor, resulting in a specific resistance of 5 – 15 Ωcm.

2.2 Substrate Cleaning

Before layer deposition the substrates must be cleaned, smoothed, and passivated, to reduce the contaminations in the deposited layers. The Si wafers are cleaned by a combination of the standard Piranha and RCA methods, which are both wet-chemical cleaning techniques that are used to free the wafer of external contaminations.

2.2.1 Piranha Solution

The Piranha solution is a mixture of sulphuric acid (H_2SO_4) and Hydrogen peroxide (H_2O_2). The chemical reaction is the following:

$$H_2SO_4 + H_2O_2 = H_3O^+ + HSO_4^- + O$$

The highly reactive atomic oxygen is responsible for the name of this solution, as it enables it to virtually 'eat up' everything, especially elemental Carbon (C) contaminations, which have proven to be very resistant towards aqueous reaction at room temperature. The Piranha cleaning is applied before the RCA cleaning to free the wafer of organic contaminations.

2.2.2 RCA Cleaning Technique

The RCA cleaning method of the Si wafer is used to free the wafer of inorganic contaminants. It is a sequential chemical oxidation in a peroxide solution H_2O_2, followed by the oxide removal in HF solution. This leaves a clean, chemically stable Si surface that is passivated by Hydrogen [23] [24]. The important point is that not only the contaminations are removed but also the naturally forming SiO_2. Si itself cannot be etched by HF. The sequence of H_2O_2 and HF dipping is repeated several times to decrease the surface roughness.
After that, the wafer is washed with a NH_4F solution to further reduce the roughness, and thereby prepare an atomically smooth Si (111) surface [25].

2.3 Film Deposition

The deposition technique of choice in microelectronics is CVD, as it allows for mass production. The technique of choice to study the fundamental behaviour and practicability of material systems is the MBE, which was used in this study for the preparation of the investigated samples.

2.3.1 Molecular Beam Epitaxy (MBE)

MBE is an acclaimed method for layer deposition, as it poses a fast, accurate, reproducible, cost effective and foremost versatile technique that serves to carry out 'proof of principle' studies.
The used MBE system (MBE DCA 600) is specified to handle 4" wafers in ultra high vacuum (UHV), and consits of a load-lock, three deposition and one analysis chambers, which are interconnected by a linear transfer system, as depicted in Fig. 6. For an introduction on vacuum systems and basic pumping principles see Ref. [26]. The three deposition chambers are for oxides (Pr_2O_3, Y_2O_3, HfO_2), group IV semiconductors (Si, Ge) and III-V semiconductors. The cleaned Si wafer is introduced into the transfer

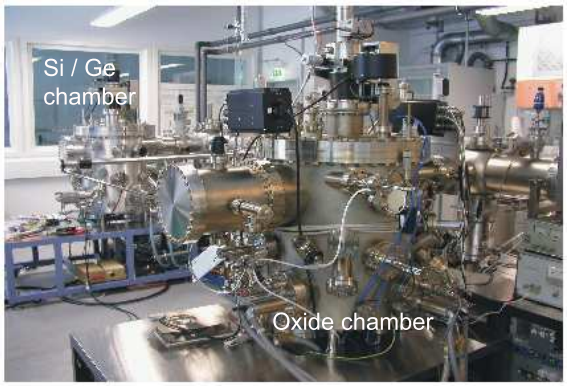

FIG. 6: UHV System containing three MBE deposition and one analysis chamber, interconnected with a linear transfer system

chamber in high vacuum (HV) (10^{-6} mbar) and degased at 200°C for 30 minutes. Then it is transferred to the UHV (10^{-10} mbar) deposition chamber.
The material to be deposited is placed in a crucible and heated by an intensive, focused electron beam. The sample is placed in the beam of the evaporated material and condensation on the sample surface forms the desired layer. There are several parameters that determine the growth rate on the sample. The flux of the atomic or molecular beam determines the number of atoms per time that arrive at the sample surface and the temperature of the sample influences the kinetics of the impacted particles. For a brief introduction to epitaxy see appendix B. In this study the sample temperature was varied by indirect heating from room temperature up to 900°C. Usually the growth rate is kept low enough to ensure a certain surface mobility. The crucibles are covered with a shutter to abruptly start and stop the deposition, furthermore the crucibles themselves are shielded to reduce the carbon contamination of the sample, coming from the crucible material, which is pyrolitic Graphite.

Before the deposition, the materials are heated for a few minutes to ensure an as continuous as possible evaporation rate. Furthermore, the sample is rotated during the entire deposition, again to cover for minor inhomogeneities of the beam. The purity of the evaporated source material, namely Ge and Pr oxide, is better than 99.99%. The pressure is kept below 10^{-7} mbar for the oxide and below 10^{-8} for the Ge during deposition in the chamber. Prior to the first deposition step, the H terminated wafer is heated up to 700°C to prepare a high quality (7x7) Si(111) surface [55]. The growth is monitored with RHEED.

2.4 The Oxide Buffer - Engineered Template for Ge Growth

As introduced in the motivation, the idea of how to integrate Ge is via an engineered oxide buffer, namely Pr oxide. The oxide is evaporated by electron beam heating in the MBE oxide chamber. The source material is Pr_6O_{11}. The oxide is chosen for various reasons, all of them permitting a high functionality. This functionality is possible because of the very complex phase diagram of the oxide. The complexity makes it possible that the properties of only one deposited material, in this study the Pr oxide, can be changed widely by adapting external parameters, even after deposition.
The oxide can be termed as engineered, because its behaviour and composition can be selected by choosing the phase. The phase again can be easily chosen by adapting temperature and oxygen partial pressure. Thereby, the parameters bound to the material phase, such as the lattice constant, the wetting behavior and interface reactivity can be altered. Along with this versatility of the oxide, a careful control of the defect densities, the stochiometry and the thermodynamic stability becomes imperative. The phase diagram of Praseodymium oxide is shown in Fig. 7. When the oxide is deposited in the MBE UHV system,

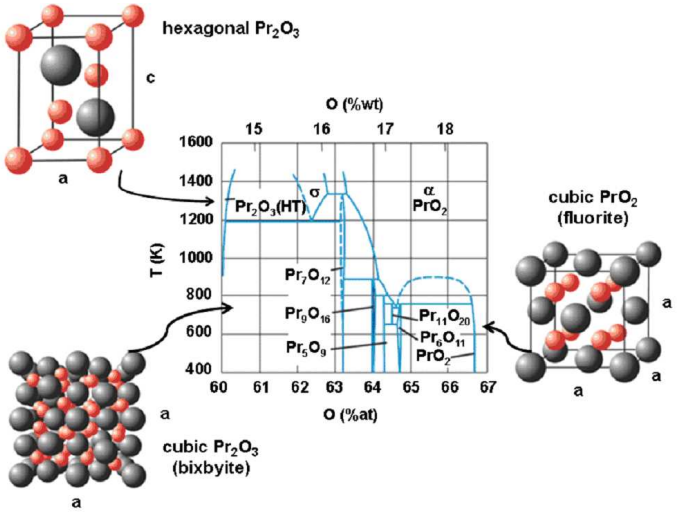

FIG. 7: Phase diagram of Praseodymium oxide [53].

the forming layer on top of the Si (111) wafer is single crystalline hexagonal Pr_2O_3 (0001). This is the best choice for the initial oxide growth, as the hexagonal phase has the smallest lattice mismatch with the Si surface (0.5%) [27, 28]. After the deposition, the wafers are taken out of the UHV system and

are annealed in an ex situ furnace. The annealing takes place in 1 bar oxygen pressure at 400°C. This induces a phase transformation from the hexagonal to cubic phase. The stochiometry is changed:

$$Pr_2O_3 + \tfrac{1}{2}O_2 \rightarrow PrO_2 \tag{2.1}$$

The thereby attained layer is twin free, type B oriented single crystalline PrO_2 (111), with a cubic Fluorite structure, which is a special case of the fcc bravais lattice with all tetrahedral voids filled [21]. The nomenclature of 'type B' orientation follows the convention in literature for the epitaxy of cubic (111) film structures grown on single crystal (111) surfaces of cubic substrates [29]. This nomenclature accounts for the circumstance that a stacking fault occurs at the Si-PrO_2 interface due to electrostatic reasons: the oxide crystal (111) stacking plane is rotated by 180° around a rotation axis that is parallel to the (111) surface normal with respect to the Si crystal. This is analogous to a 3D coordinate system transformation obeying the rules of a linear transformation. This causes all vectors in-plane of the (111) planes of the oxide and the Si substrate to be anti-parallel (e.g.:$[11\bar{2}]_{Si} \| [\overline{11}2]_{PrO_2}$).
This oxide has three main advantages:

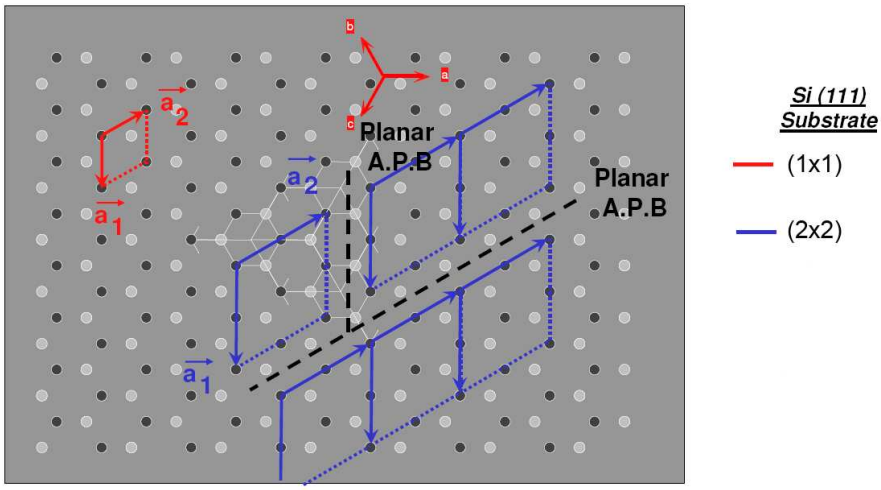

FIG. 8: The Si (111) surface. Two overstructures are indicated (1x1) (blue) and (2x2) (red) [30].

1. The lattice constant is almost matched with Si, allowing for a (1x1) coincidence lattice on the Si surface. This reduces the geometrical misfit induced strain.

2. The cubic fcc structure allows for the transportation of the stacking information and thus prevents the formation of twins in the Ge epi-layer[1].

3. In the cubic Fluorite structure all tetrahedal voids are occupied by Oxygen, preventing the formation of both anion as well as cation anti phase boundaries (APB's) [31]. As shown in Fig. 8, the coalecense of (1x1) overstructured oxide islands (red arrows) on the topmost Si atom layer (black spots) cannot cause the appearence of APB's. In a (2x2) overstructured oxide the lattice nuclei

[1] This is coroborated in the results part of this thesis.

(blue arrows) do not have to coincide, this can result in the formation of APB's as indicated by the dashed lines.

2.5 Film Characterization Techniques

Various techniques are applied to characterize the deposited films in- and ex-situ. They are briefly described in the following:

2.5.1 X-Ray Diffraction (XRD)

XRD utilizes x-rays to study material and structural properties. Its major advantage is the non destructive depth information on the probed samples. The penetration and thereby information depth of x-rays is following the Lambert-Beer law of absorption and is experimentally in the range of several hundred micrometers. In x-ray techniques there is always an averaging over a comparatively large area, typically in the range of cm^2. Smaller beam sizes are possible in micro beam focus specialized beamlines at some synchrotons. The diffractometers used in this thesis are:

– Laboratory based Rigaku DMAX 1600:
This is a diffractometer of the Bragg Brentano type. The vertically mounted sample is irradiated by Cu (K_α) radiation ($\lambda = 1.56\,\text{Å}$) from a rotating Copper anode. The characteristic radiation of one element has a well defined linewidth, but is isotropic and therefore needs to be focused in order to improve the intensity. The most common focusing geometry in use is named after its inventors "Bragg-Brentano". Source and detector are placed on a circle that is centered around the sample. The source position is fixed and the sample is tilted at an angle θ and the detector at 2θ with respect to the incoming beam (see Fig. 9). Before the detector, the diffracted intensities

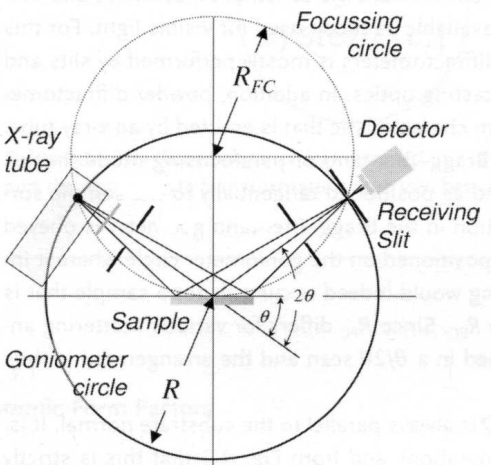

FIG. 9: Top view of a Bragg Brentano diffractometer geometry [32]

pass a Graphite monochromator to separate the diffracted K_α radiation from the also diffracted K_β

radiation, as well as to reduce the background. The $K_{\alpha 1}$ line cannot be separated from the $K_{\alpha 2}$ line by this setup, in consequence the recorded laboratory spectra always exhibit a double peak structure. The detection of the diffracted intensities over the corresponding detector angle is the recorded information. The typical range for a specular $\theta - 2\theta$ measurement is from 20° to 120°. For the occurence of diffraction at all, a very high crystalline order is necessary. As introduced in basic solid state physics, the lattice d-spacing in a single crystal has the following relation to the reciprocal lattice vector,

$$d_{hkl} = H_{hkl}^{-1} \tag{2.2}$$

which leads to the famous Bragg's law, visualized in Fig. (10):

$$\frac{\vec{s} - \vec{s}_0}{\lambda} = \vec{H}_{hkl} \tag{2.3}$$

with $\vec{s}$ the unity scattering vector in the sample-detector direction, $\vec{s_0}$ the scattering vector in the source-sample direction, λ the wavelength of the incoming beam and $\vec{H}_{hkl}$ the reciprocal lattice vector. It states that only for those impulse transfer vectors constructive interference is possible, for which it is equal to a reciprocal lattice vector. The intensity distribution from different lattice planes given by kinematical scattering is derived in more detail in appendix A. The scattering conditions are given by the geometrical setup, which only permits specular scans, it only allows for the detection of lattice planes oriented parallel to the surface. The investigated samples were Si (111) substrates, therefore only diffracted intensities from lattice planes parallel to the Si (111) planes are detected with this diffractometer. If there are more diffraction signals than expected from the single crystalline lattice in the epi-layers, the layers are not single-, but poly crystalline.

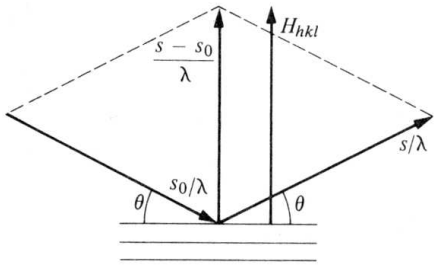

FIG. 10: Diffraction condition on lattice planes for positive interference [33]

– Laboratory based Rigaku Smart lab:
With this diffractometer both in-plane as well as pole figure measurements are possible in addition. For the in-plane measurements, the sample is mounted horizontally and the sample is irradiated under grazing incidence (the incidence angle (α_i) typically varies between 0° and 0.6°). Then again, the sample is rotated by θ and the detector by 2θ. The difference with respect to specular scans is that the sample is rotated around the (111) surface normal and the surface normals of planes that give rise to diffracted intensities are perpendicular to the Si (111) surface. A further asset of this kind of measurement is that not only the additional in-plane information is gained, but also the information depth can be adapted by changing the angle of incidence. The angle can be chosen with regard to the critical angles of the different material layers. If the critical layer of

an epi-layer is reached, total reflection occurs and the diffraction spectra contain only information about the material on top of the layer, for which the critical angle was fallen short of.
Pole figure measurements are in principle nothing else but θ-2θ measurements for one certain lattice d-spacing, for all possible angular orientations of the sample. As the specular θ-2θ measurement, they are bulk sensitive. This means the source and the detector are placed at one certain diffraction condition, namely the 2θ angle, and the sample is rotated around the diffractometer angles α and β, as shown for the Smart Lab in Fig. 11. This allows for the detection of lattice

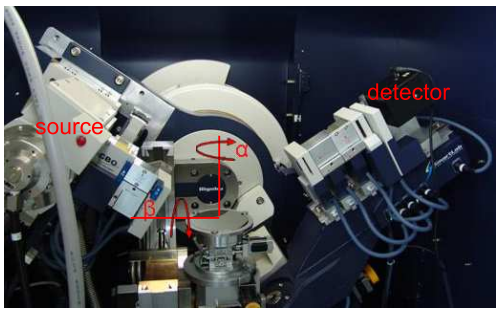

FIG. 11: Rigaku Smart Lab. Pole figure coordinates as depicted.

planes with the same multiplicity (and therefore d-spacing in cubic systems), or simply the detection of lattice planes with a certain d-spacing, misaligned within the crystal. The principle of a pole figure is the two dimensional representation of the three dimensionally distributed diffraction signals. The sample is in the center of a sphere given by the detector of the diffractometer. On this sphere, a 'north' and 'south' pole are defined. The detected intensities on the 'northern' half of the sphere are projected onto the south pole. The intersections of the plane, separating northern and southern half-sphere, and the projection lines create the pole figure. This geometrical, angle true projection is also referred to as stereographic projection. While a pole figure contains only the projections from one hemisphere onto one pole, the stereographic projection includes all intersections of projections of both hemispheres onto both, the north and south pole.

– HASYLAB synchrotron beamline BW 2 / ESRF beamline ID 32:
Synchrotron radiation has the advantage that it is truly monochromatic, highly coherent radiation with very little dispersion. The peaks in synchrotron recorded spectra thus do no exhibit the double peak feature as for Cu radiation used in the laboratory based diffractometers. The intensity is several orders of magnitude higher than for laboratory based diffractometers. The detection of very weak signals that vanish within the background in laboratory based measurements is therefore possible. Furthermore, the diffractometers at BW 2 and ID 32 allow not only for specular and in-plane measurements but also for off-plane measurements. In those off-plane scans, the diffraction from lattice planes with an arbitrary angular relationship to the surface is detectable. In summary, all laboratory based measurements are also possible at the synchrotron. The different scans of the epitaxial layer systems carried out are:

1. Specular scans:
   Investigating the stacking in the vertical grown direction (see Fig. 12(a)).

2. In-plane scans:
   Investigating the azimuthal orientation perpendicular to the surface. The azimutal film orientations with respect to each other can be determined (see Fig. 12(b)).

3. Off-plane scans:
   Investigating the general stacking as both the vertical and azimuthal crystal information is included (see Fig. 12(c)).

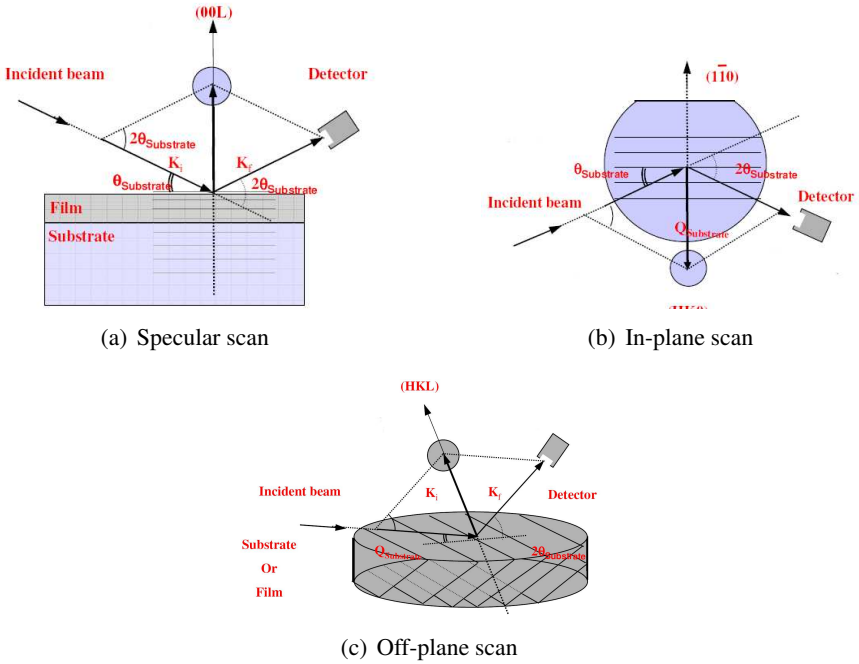

(a) Specular scan

(b) In-plane scan

(c) Off-plane scan

FIG. 12: Different scans carried out at the synchrotron beamlines to determine epitaxial relationship [30]. The faint black lines in the substrate and the film indicate the lattice planes at which the x-ray beam is diffracted.

2.5.2 X-Ray Reflectivity (XRR)

The in this thesis presented reflectivity curves are specular reflectivity curves. Specular x-ray reflectivity is used to measure thin film thicknesses, interface roughness and layer density. There is no difference in the optics of visible light and x-rays, the only distinction is that the refractive index (n) is different. For the measurement of x-ray reflectivity, the same setup as described for the XRD measurements with the Rigaku DMAX is used, but the typically measured angular range for 2θ is between 0° and 8°. The technique is unable to discriminate between amorphous layers and layers with crystalline order. The index of refraction for x-rays is:

$$n = 1 - \delta - i\beta \tag{2.4}$$

δ is always smaller than 1 and β is always smaller than δ. Therefore n is always smaller than 1 for x-rays, in contrast to visible light where it is always bigger than 1. The index of refraction is a function of the

electric susceptibility, and the latter again a function of the charge density. As each material has a unique electron density, n is a material characteristic. The deviation from 1 contains the information about the reflecting layers. The recorded information is likewise the reflected intensity over the corresponding 2θ angle. The XRR spectra can be separated into three parts [32], as shown in Fig. 13: an increasing part (I), a plateau (II) and a rapidly decreasing part (III). The ratio of the reflected intensity to the intensity of

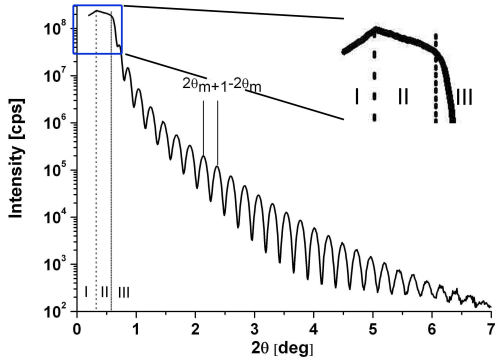

FIG. 13: Typical logarithmic reflectivity profile. The probed sample is a Si(111) wafer covered with a 10nm thick PrO_2 layer

the incomming beam can be derived from the Fresnel coefficients, resulting in:

$$\frac{I_R}{I_0} = \left| \frac{\theta - \sqrt{\theta^2 - \theta_c^2 - 2i\beta}}{\theta + \sqrt{\theta^2 - \theta_c^2 - 2i\beta}} \right|^2 \tag{2.5}$$

with the angle of incidence θ and the critical angle θ_c below which total external reflection occurs. In region I (Fig. 13), the irradiated area is even bigger than the sample, resulting in an increase of the intensity with an increasing angle of incidence. The reflected intensity reaches its maximum when the irradiated area is as big as the sample. At this point, region II is reached, in which the reflected intensity is almost constant. For the corresponding angles, the critical angle is fallen short of. When the critical angle is reached, the intensity decreases with a so-called Parod slope $\left(\frac{1}{(\vec{k}-\vec{k_0})^4} = (\frac{4\pi\lambda}{\sin\theta})^4\right)$, as described in the literature [32]. For interface and surface roughness, an additional exponential damping is observable. This makes it possible to simulate surface and interface roughness according to the recorded damping of the intensity.

The most striking feature of the reflectivity curve is the intensity oscillation observed in region III. These "Kiessig" fringes are a thin film effect [34]. In the depicted case, they are due to a thin PrO_2 film on top of the Si substrate ($d \approx 10$ nm). The maxima of these oscillations occur, if the path difference of reflected and refracted (in the PrO_2 layer) beam is equal to a multiple integer of the wavelength. From a close inspection of the geometry of reflected, refracted beams and the corresponding angles it is seen that

$$2\theta_{m+1} - 2\theta_m \approx \frac{\lambda}{d} \tag{2.6}$$

i.e., the distance of two adjacent oscillation maxima is approximately the wavelength of the beam divided by the thickness of the layer (d). In the simulation of the spectra, the thickness of the layer, the surface roughness, and the electron density are used as a parameter and fitted accordingly.

Nowadays, most commonly recorded reflectivity curves are fitted with a software, and d is used as a parameter in the fit. The program used for the evaluation of the XRR spectra is RCRefSim [35]. More information on reflectivity can be found in [36].

2.5.3 Reflection High Energy Electron Diffraction (RHEED)

RHEED is used to monitor the growth of the layers in-situ in the MBE. In RHEED, a high energy electron beam (acceleration voltages $U = 10kV - 30kV$) is directed onto the crystal surface under grazing incidence. The angle of incidence (typically $\alpha_i = 0.5^\circ - 2.5^\circ$) is arranged in such a way that the penetration depth is as small as possible and the influence of the surface on the diffraction maximized. In the first approximation to derive RHEED pattern, the following simplifications are made:

1. The scattering of the electrons at the surface mesh is considered to be kinematical; only single scattering events are taken into account. The electrons are assumed to be nonrelativistic.

2. The scattering is assumed to be elastic: $\vec{k} = \vec{k_0}$. Inelastic scattering yields to better results, but the deviations caused by, for example, plasmon scattering are only detectable with high resolution equipment.

3. Following basic kinematic scattering theory (see introduction to XRD) the impulse transfer vector must be equal to a reciprocal lattice vector to fulfill the Bragg condition:

$$\vec{H_{hkl}} = \vec{k} - \vec{k_0} \tag{2.7}$$

Due to the glancing incidence angle and the strong electric interaction of the electrons and the shells of the material atoms, only the topmost layers are probed. The crystal below the surface can be neglected. As the real space becomes a two dimensional mesh by this condition, the reciprocal space becomes a set of rods oriented along the surface normal direction (z direction). The intuitive concept of the Ewald sphere can be used to explain the diffraction: The wavevector is given by the de Broglie relation

$$\vec{p} = \hbar\vec{k} \tag{2.8}$$

and is therefore proportional to the energy. As the radius of the Ewald sphere is given by k, it is much larger than the smallest reciprocal lattice vector, and a large region of the reciprocal space is probed. Due to natural imperfections of the experiment, the Ewald sphere is rather a spherical shell with a finite thickness. The rods of the reciprocal surface mesh exhibit a finite size as well. In consequence, the

intersections of the finite crystal truncation rods on the surface mesh with the Ewald sphere 'shell' give a streak that is observable for atomically smooth surfaces. The diffracted electrons are observed on a fluorescence screen and recorded by a camera. The experimental setup as well as the diffraction conditions are shown in Fig. 14. The intensity distribution and spot shape are completely given by the kinematical

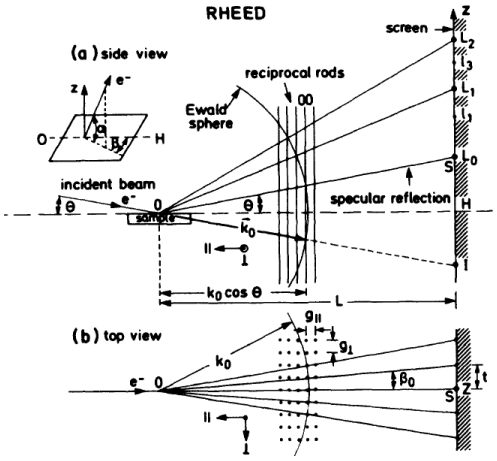

FIG. 14: RHEED setup and Ewald sphere construction. The projection of the intersections with the truncation rods gives the intensity maxima on the fluorescence screen [37]

scattering, which is calculated for x-ray diffraction in appendix A. In comparison, dynamical scattering theory predicts the complete intensity distribution, i.e., intensity quantification. For the understanding of the relative and absolute intensites, dynamical scattering theory is needed, which is not treated in this thesis. A good insight into RHEED experiment and theory is given by [38].
The RHEED patterns presented are taken with Staib Instruments RHEED 30WSI and fluorescence screens mounted in both, the oxide and the SiGe chamber of the DCA MBE, with an identical RHEED set-up.

2.5.4 Electron Microscopy

1. **Transmission Electron Microscope** (TEM):
   Is the preeminent method in material science for the imaging of the crystal morphology, the crystal phases, as well as dislocations and defects, as it allows for high resolution lattice imaging in real space. It can be used for the display of reciprocal planar cross sections, i.e., diffraction patterns, or the real space image of the sample. A very well focused electron beam is transmitted through the thinned sample and the electrons are detected behind the sample. The electrons are accellerated to a several hundred keV (a typical acceleration Voltage is 200 kV). The resolution limit of the tool is given by the electron wavelength:

$$d = \frac{\lambda}{2\beta} = \frac{0.6\ nm}{\beta\sqrt{V}} \tag{2.9}$$

In principle, the resolution is sub atomic (0.2 Å), but optical abberation correction effects limit the resolution to $\approx$ 1 Å. There are different imaging modes, dependent upon which transmitted electrons are selected for imaging, e.g., in a phase contrast image two or more diffracted beams are used to form the image. The biggest drawback of the TEM is the destructive sample preparation: Electrons must be transmitted through the sample, therefore the samples must be thinned by ion milling. The TEM images presented in this thesis were obtained using a Philips CM 300 (300 keV) microscope with a point to point resolution of 1.8 Å. Images with an atomic resolution are also often called High Resolution TEM (HRTEM) images.

2. **Scanning Electron Microscope** (SEM):
   In a SEM, the sample is scanned with a highly focused electron beam with high energy. The energy ranges from 100 eV to several 100 keV. The number of the back-scattered electrons from the primary beam, as well as the number of secondary electrons created during the scan in the probed material, are a function of the topography of the sample and the local material constitution. In the most common detection mode, the back-scattered and secondary electrons are detected as a function of the primary beam position and an image is formed. The resolution is limited to about 2 nm, and thus smaller than for TEM, but contains a very large depth information with a high depth of field, enabling the imaging of three dimensional structures. This is the case for some of the presented images in the following. The technique is also used in microelectronics for electron beam lithography to create structures in the nm regime on the Si wafer.

3 Results and Discussion

3.1 Structure

In the following, the development of the growth of closed Ge layers, as well as a thorough discussion of the epitaxy of the closed Ge layers is given.

3.1.1 Development of the Growth Recipe for Closed Ge Films

The 4" Si wafer, covered with phase transformed cubic PrO_2, is reintroduced into the MBE system, and transferred to the Ge chamber. The wafer is heated to various temperatures, at which Ge is deposited. During the heating, the RHEED pattern of the cubic PrO_2 exhibits a 4x4 overstructure for temperatures above 400°C with respect to Si (111). The deposition of the Ge layer takes place in two subsequent steps:

1. Deposition of a thin seed layer at 600°C, needed for single crystallinity and type A epitaxy. For lower deposition temperatures, the deposited layer is highly twinned, i.e. not single crystalline. The deposition time for the seed layer is 100 s.

2. Deposition of a smooth Ge layer onto the single crystalline epitaxial template (seed layer). In this step, the flux of the arriving Ge atoms and the temperature of the substrate are varied.

It should be noted that such a two stepped deposition has also been reported for Ge on $SrHfO_3$ [39]. The experiments in this study are summarized by Fig. 15. Among the prepared samples, the presented four are selected for reasons of clearness, as they represent the main results of the variation of the second step of the growth recipe. The results of the experiments are discussed by one result for each quadrant. The substrate temperature is given in °C and the filament current of the Ge source has been selected as a measure for the Ge flux, which is given in mA. The given values of 60 mA and 90 mA represent the limits with respect to experimentally reproducible flux conditions. Since the growth rate in Å/min is not only dependent on the current from the heating filament, but also from the substrate temperature, this rate can only be calculated from ex-post measurements of the layer thickness. For each sample, the information is given by four pictures, namely the evolution of the RHEED pattern along a stacking sensitive <1$\bar{1}$0> azimuth of the Si (111) wafer and a SEM image of the final layer after deposition. The white arrows in the RHEED patterns indicate the position of the [00L] streak.

Step one of the Growth Recipe - the Ge Seed Layer:
The first group of images, Fig. 15-(A1+B1+C1+D1), are the recorded diffraction patterns of the PrO_2 oxide buffer surface of each sample before deposition, recorded at 600°C. The streaks indicate the smoothness of the oxide surface, although a limited roughness is present, as indicated by the slight intensity modulation along the streaks. For completeness it should be remarked that in some images, a faint (4x4)

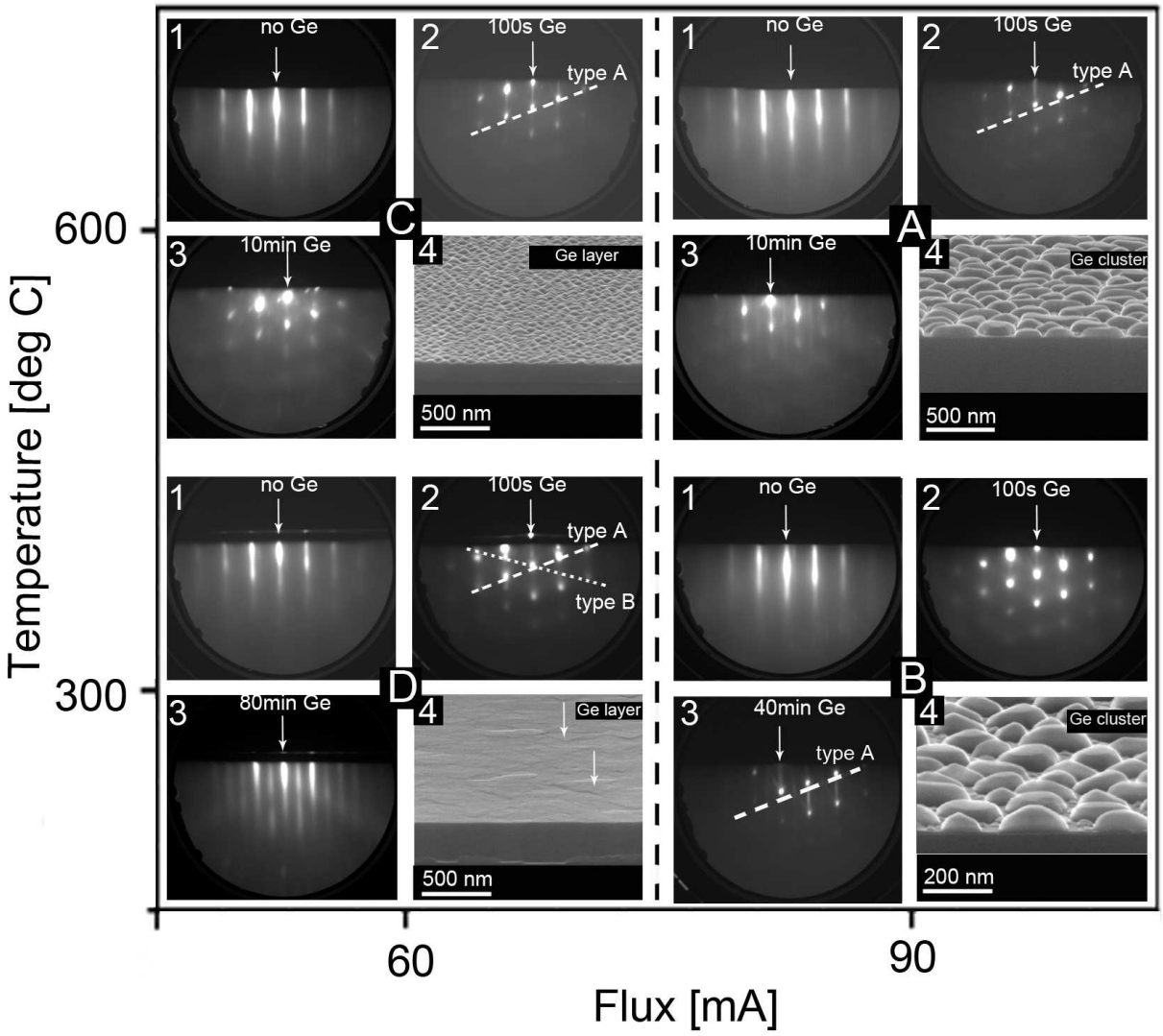

FIG. 15: Four representative samples for the discussion of the influence of flux and temperature on growth conditions.

overstructure is visible, after heating the oxide above 450 °C. When the Ge deposition starts, the pattern becomes at first more diffuse, and after several seconds very spotty, i.e., along the streaks spots become visible, as can be seen in the second group of images, Fig.(15)-(A2+B2+C2+D2). The increase of the background can be attributed to a complex chemical interface reaction that causes the formation of highly volatile GeO_2. This reaction at the interface causes a reduction of the oxide to cubic Pr_2O_3. For a more detailed discussion of the initial growth behaviour of Ge on the PrO_2 oxide support system see [22]. The spots clearly indicate an initial Volmer-Weber growth mode of Ge on the reduced Pr_2O_3 (111) support. The asymmetric arrangement of the Bragg peaks on parallel lines (one of those indicated by the dashed line and marked with "type A") is typical for (111) oriented fluorite crystal structures imaged along the $<1\bar{1}0>$ azimuth [40]. A close inspection of the spot positions after the deposition of the seed layer exhibits the weakly visible presence of a mirror symmetry in the pattern Fig. 15-(A2+B2+C2+D2), e.g., the first spot along the [01L] streak is also visible along the [$0\bar{1}$L] rod, as specially emphasized as "type

B" in Fig. 15-(D2). As both the oxide as well as the Ge have a fcc related crystal structure, the hardly visible type B spots can be due to either diffraction on the oxide surface, not covered by Ge islands, or it might be Ge twins forming at the interface. The defect behaviour is discussed in detail in the defect part of the results.

Step two of the Growth Recipe - Variable Flux and Temperature:

As the results for this step differ very much for each sample, the discussion begins with constant flux starting at 600°C, and moving down to 300°C. This is repeated for the discussion at a flux of 60 mA. The sequence which the discussion follows is A → B, → C → D.

For the sample deposited at high temperature and high flux (A: 600°C / 90 mA), the RHEED pattern is still spotty (Fig. 15-(A3)) after 10 min of Ge deposition, indicating that the islands do not form a closed layer, or do form a closed layer with a rough surface in the range of several nm. As the RHEED is only surface sensitive, a coalescence of the islands cannot be excluded by the pattern alone, as islanding cannot be distinguished from surface roughness. The pattern is a pure type A Ge Bragg pattern. A weakly visible surface reconstruction is present, which might be a Ge c(2x8) surface reconstruction [41]. The SEM image of Fig. 15-(A4) shows the final layer at a scale of 500 nm, corresponding to the diffraction pattern of Fig. 15-(A3). The Ge islands are clearly visible. The spots in the RHEED pattern therefore cannot be attributed to the surface roughness of a closed Ge layer. The ordering of the Ge islands seems to be arbitrary, thus an ordering of nucleation centers is unlikely, but cannot be excluded. The average lateral size of the islands is around 275 nm.[2]

For the sample deposited at low temperature and high flux (B: 300°C / 90 mA), the RHEED pattern after 40 min of Ge deposition stays spotty as well Fig. 15-(B3). Fig. 15-(B4) shows the SEM image of the final sample on a scale of 200 nm. As for the higher flux Ge islands are clearly visible, which do not systematically coalesce. The average lateral size of the islands is around 157 nm.

For the sample deposited at high temperature and low flux (C: 600°C / 60 mA), the RHEED pattern remains again spotty after 10 min of Ge deposition. The ex-situ SEM image of Fig. 15-(C4) reveals now that, contrary to the results for the samples grown at high temperature, the Ge layer is closed. The growth that started at the nucleation sites formed coalesced islands. The final film is closed, at least on the given 500 nm scale. Nevertheless, the surface is still very rough.

The final result for the sample deposited at low temperature and low flux (D: 300°C / 60 mA) is that even after 10 min of Ge deposition the spots in the RHEED pattern start to disappear (not shown). The RHEED pattern shows these streaks after a deposition time of 40 min, indicating a smooth surface (Fig. 15-(D3)). The presented SEM image (Fig. 15-(D4)) is from a sample grown under the same conditions, but with a prolonged deposition time at 300°C, on a scale of 300 nm. The closed layer is evident. Even the threefold symmetry of (111) surfaces in fcc lattices can be seen by the presence of triangles on the surface, two of

[2] A grazing incidence small angle x-ray scattering (GISAXS) study of this sample shows a preferential behaviour of the island shape and ordering of the nucleation centers very well. The general results will be published elsewhere. The average island size for all samples discussed is calculated from the GISAXS data. A detailed study of an almost identical system did show an order of the nucleation sites [20].

which are highlighted by white arrows.

Discussion:

In conclusion, growth parameters have been found that result in the desired closed and single crystalline (will be shown in the following) Ge layers. The initial growth mode at high temperature is Volmer-Weber (see appendix B). The layers were not achieved by changing the growth mode from Volmer-Weber to van der Merwe, but by a smoothening out of the Volmer-Weber growth, shown in Fig. 16. This is discussed in detail by our group in [22].

The physics behind the two steps of the growth recipe can be understood as:

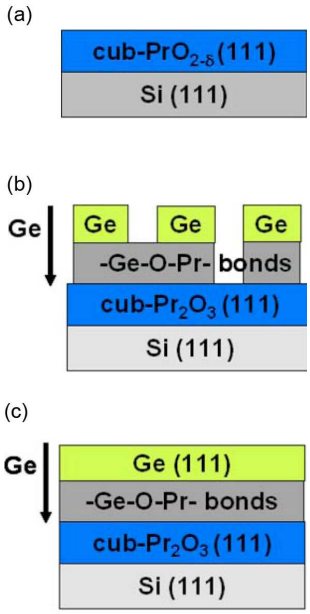

FIG. 16: The development of the Ge layer growth with deposition time. From the initial Volmer-Weber growth to the final smooth layer.

1. **High temperature seed layer deposition – epitaxial growth:**

   This is the initial deposition of the Ge on the Pr_2O_3 / Si template. Epitaxial growth takes place, governed by the functional dependence of the chemical potential. This is the important variable in epitaxial growth, i.e., its functional dependence on surface and strain energies, interface interactions and temperature determine the growth mode (see appendix B).

   The wetting behaviour of the entire Ge on the wafer observed follows a Volmer-Weber growth mode and is a consequence of the decreasing chemical potential with the distance to the Ge / Pr_2O_3 interface, given by the interface and strain as well as surface energy of each layer. For the bonding of Ge and Pr_2O_3 at the interface, as well as the surface, and strain energies, no other growth mode than Volmer-Weber seems to be thermodynamically possible. This points to stronger inner Ge - Ge bonds than the Ge - Pr_2O_3 bonding at the interface, and thus a low interface energy. Furthermore, the Ge surface energies are apparently low enough to allow for a Ge island growth, as can be seen by the introduction of additional facets in the formation of islands.

The detailed inspection of the structure of each island reveals information on its strain state. The Ge layer has a misfit with the underlying oxide buffer. There are two possibilities for the layer system to relax the misfit induced strain: Firstly plastic relaxation and secondly elastic relaxation. In plastic relaxation, defects (i.e. misfit dislocations and thus strain fields) are introduced in the island.

In elastic relaxation, no defects are introduced in the islands, but additional surface is created by the macerating of each island.

The Ge islands on the oxide, growing by Volmer-Weber growth mode, have been shown to be fully relaxed and mostly dislocation-free for a sample grown at only the seed layer deposition conditions [20]. Furthermore, this study revealed the formation of for instance {113} and {110} facets, which are energetically higher than the (111) surface, as this surface has the lowest surface energy [42]. Therefore, an elastic relaxation of the Ge seed layer can be assumed to be the dominant process in the relaxation of the misfit induced strain.

For completeness, it should be noted that the bigger average island shape for the higher flux is explainable by the fact that the progression of the island size increases linearily with the rate of the incoming atoms.

2. **Low temperature deposition – crystal gowth:**

   As the Ge islands are fully relaxed, the growth is not dominated by the thermodynamics of the interface but rather a case of crystal growth of the same species. Starting on the seed layer, the Ge islands are oriented vertically in (111) direction, but have additional facets. These additional facets are not the energetic minimum, accordingly the system tends to its energetic minimum, which is the Ge (111) surface. The relaxation to the (111) facet is easier at lower temperatures as the facets with higher surface energy are not activated, and the system is able to relax into its thermodynamic equilibrium state. The following coalescence of the Ge grains of each island resulting in the Ge layer only takes place with the introduction of defects, yielding to the layer quality described in the following sections.

Summarized, the behaviour of the Ge deposit in general fits well into the theory of epitaxial growth, but is more complicated due to the complex interface reaction of the Ge and the oxide, as well as the behaviour of the nanoscaled oxide buffer.

3.1.2 Structure Study and Epitaxial Relationship of the Heterostack

All of the results presented belong to one Ge (111) / Pr_2O_3 (111) / Si (111) sample obtained under closed Ge film growth conditions, i.e., a Ge deposition rate of 0.8 nm / min. If results are taken from other samples it is specially emphasized.

Specular $\theta - 2\theta$ Measurements:
The thickness has been determined with XRR. The recorded XRR curve of the exemplary sample with the corresponding fit is given in Fig. 17(a). The recorded intensity is given in log scale, while the angle is given in degree. The data points of the measurement are the black line, the fit is represented by the red line. The parameters of the fit are: thickness, electron densities and surface / interface roughnesses. The fit has been vertically displaced on purpose to visualize the excellent coincidence of the experimental data points with the fit. In Fig. 17(a), there is a beat of two different frequencies visible. The one with the larger period belongs to the thinner Pr_2O_3 layer and is visible even above 8°. The one with the smaller period belongs to the much thicker Ge layer. The Ge layer oscillations vanish around 6°, which points to a higher roughness in comparison with the Pr_2O_3 layer roughness. The model that has been used to fit to the data assumes two layers, on a fixed Si substrate, namely the Pr_2O_3 layer and one subsequent Ge layer. The fact that Ge layer oscillations are observable, corroborate the SEM findings of a closed Ge layer. The fit results are: The Ge layer has a total thickness of 83 nm, the Pr_2O_3 layer $\approx$ 9 nm,

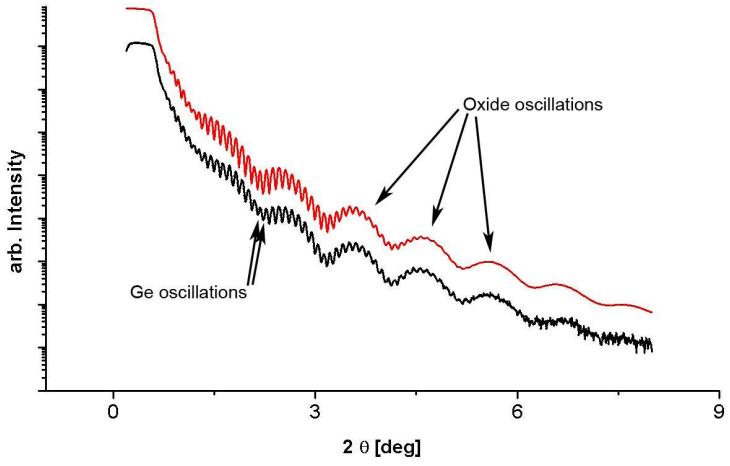

(a) Recorded reflectivity over angle (black), and fit (red), displaced to show coincidence

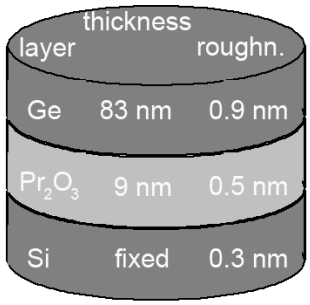

(b) Results of the fitting procedure

FIG. 17: Measurement of the reflectivity, displayed with the fit and its results

while the Si substrate is fixed, and not considered as a fitting parameter. The surface roughness (rms) of the epi-Ge layer is about 0.9 nm, while the interface of the oxide and epi-Ge amounts about to 0.5 nm, and the interface of the oxide with the Si substrate about 0.3 nm. The relative densities of the layers (not shown) are close to the bulk values (where 100 % would be equal to the bulk value) with 97 % for the epi-Ge layer and 98 % for the Pr_2O_3 layer. In comparison with the local information (1 μm^2) given

by the presented SEM images, the obtained information is here an average over the area of cm^2, which corresponds to the illuminated area of the incident x-ray beam. Thus the information is highly averaged and considered as representative for the entire sample.

The vertical growth direction of the Ge / Pr_2O_3 heterostructure on Si was controlled by specular $\theta - 2\theta$ scans. The scan is given in Fig. 18. The intensiy is given in logarithmic scale, while the angle is given in degree. The scan shows only Bragg peaks due to lattice planes parallel to the Si (111) surface. For this system, there are exactly three peaks expected for each of the layers and the Si wafer in the scan range of 20° – 105°, namely the (111), (222) and (333) reflection for the Ge layer and the Si wafer. For the Pr_2O_3 layer, the (222), (444) and (666) reflections are expected, accounting for the almost two times bigger bulk cubic lattice constant of the oxide with respect to Si.

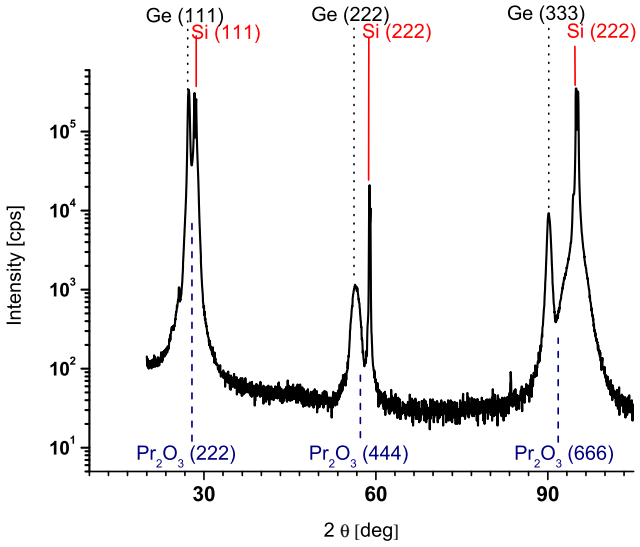

FIG. 18: XRD spectra of the closed Ge film sample. The bulk peak positions are marked with lines.

Layer	Bulk Angle [deg]	Bulk d-spacing [Å]	Angle [deg]	d-spacing [Å]
Ge (111)	27.28	3.27	27.3	3.26
Ge (222)	56.39	1.63		
Ge (333)	90.07	1.09	90.10	1.08
Pr_2O_3 (222)	27.69	3.22		
Pr_2O_3 (444)	57.18	1.60	56.40	1.62
Pr_2O_3 (666)	91.75	1.07		
Si (111)	28.44	3.12	28.44	3.12
Si (222)	58.87	1.57	58.87	1.57
Si (333)	94.97	1.05	94.97	1.05

In the scan, strong signals are visible close to the Si (111), (222) and (333) reflections. The Si (111) and (333) reflections exactly match with the angular positions of the strong peaks at around 28° and 94° with their bulk values. The strong reflection around 58° matches with the theoretical value of the Si (222) reflection. The intensity is around two orders of magnitude lower. This is due to the fact that the (222) reflection is forbidden in a diamond lattice (see Appendix A). Those peaks can be therefore unambigiously assigned to the Si {111} netplane reflections. The corresponding Ge (111) and (333) reflections are found close to the Si reflections at their theoretical values, within the resolution limit of the diffractometer. The (222) and (666) oxide reflections are not visible as seperate Bragg peaks in the scan. As the oxide is only $\approx$ 8 nm thick, the intensity is several orders of magnitude smaller compared to the Ge and Si reflections and might thus be superimposed by the semiconductor reflections. It is also possible that they are shifted due to a distortion of the cubic lattice caused by the misfit induced strain. The position of the broader peak close to the Si (222) (at θ=56.4°) reflection is almost the one expected for the Ge (222) reflection. Nevertheless, a detailed study of the tetragonal distortion of the cubic bixbyite structure of Pr_2O_3 in this very system revealed that this peak is actually the Pr_2O_3 (444) reflection [43]. As all visible peaks are accounted for, the vertical growth direction of the heterostructure is deduced, i.e., the (111) surface normals of each layer are parallel. For the deduction of single crystallinity, a full three dimensional x-ray characterisation must be undertaken. Therefore, the specular $\theta - 2\theta$ scans are supplemented by in-plane and out-of-plane scans.

In-Plane Measurements:

To gather information on the in-plane and out-of-plane orientation of the oxide as well as the Ge film, surface and bulk sensitive synchrotron based GIXRD measurements were carried out. The scans were repeated for different angles of incidence, varied from 0.6° to 0.1°. The beam energy was adjusted to 10.7 keV, at which the critical angles for Ge and Pr_2O_3 are α_c=0.22° and 0.26°, respectively. For angles of incidence smaller than the critical angle of the material, the attenuation length is drastically decreased, and in principle information of the layers below the one, for which the critical angle was fallen short of, can be suppressed. For example, the attenuation length of the x-ray beam at 10.7 keV in Pr_2O_3 is for the incident angle of 0.6° (above α_c=0.26) around 100 nm and for 0.2° (below α_c=0.26) only around 8 nm. The Bragg peaks are indexed with respect to the bulk lattice (cubic coordinate system), as well as in the hexagonal Si (111) surface coordinate system. The latter coordinate system is most convenient for GIXRD measurements, because with a proper calibration the measured hkl values can be taken directly for the calculation of the lattice d-spacing [33]. In addition, it has the advantage that in the measurement of crystal truncation rods (out-of-plane scans), the values for h and k are integers, while l is scanned along. For in-plane measurements along one of the high symmetry directions of Si(111), i.e., the $[1\bar{1}0]$ or $[11\bar{2}]$ directions, the scan is just along h, or h=k, respectively. The transformation from cubic bulk coordinates to hexagonal Si (111) surface coordinates can be derived from the real space surface unit cell, spanned by the lattice vectors:

$$\vec{a}_1 = \tfrac{1}{2}\cdot\begin{bmatrix}1\\0\\\bar{1}\end{bmatrix}\cdot a_{\mathrm{cubSi}}, \qquad \vec{a}_2 = \tfrac{1}{2}\cdot\begin{bmatrix}\bar{1}\\1\\0\end{bmatrix}\cdot a_{\mathrm{cubSi}}, \qquad \vec{a}_3 = \tfrac{1}{3}\cdot\begin{bmatrix}1\\1\\1\end{bmatrix}\cdot a_{\mathrm{cubSi}}$$

Following the basic definitions for the construction of the corresponding reciprocal space Si (111) surface unit cell, the transformation matrix from reciprocal cubic bulk to reciprocal hexagonal surface coordinates becomes:

$$\begin{bmatrix}h\\k\\l\end{bmatrix}^{\mathrm{bulk}} = \frac{1}{6}\begin{bmatrix}4 & -4 & 6\\4 & 8 & 6\\-8 & -4 & 6\end{bmatrix}\cdot\begin{bmatrix}h\\k\\l\end{bmatrix}^{\mathrm{surf}} \tag{3.1}$$

Now the above claimed convenience is obvious, as for instance the [h00] surface direction is parallel to the $[11\bar{2}]$ high symmetry direction of the bulk crystal. This transformation is also valid for the transformation of Ge bulk coordinates into the hexagonal Ge (111) surface system, as they have the same space symmetry group, with only different lattice constants. This transformation is not correct for the bulk lattice of Pr_2O_3, although it is a cubic structure, as it has a two times bigger lattice constant, as well as a stacking fault at the Si interface that causes a rotation of the lattice (and along with that its cubic coordinate system) by $\frac{\pi}{2}$ around the [111] surface normal direction. The correct transformation matrix is for the oxide:

$$\begin{bmatrix}h\\k\\l\end{bmatrix}^{\mathrm{bulk}} = \frac{1}{3}\begin{bmatrix}-4 & 4 & 6\\-4 & -8 & 6\\8 & 4 & 6\end{bmatrix}\cdot\begin{bmatrix}h\\k\\l\end{bmatrix}^{\mathrm{surf}} \tag{3.2}$$

Fig. 19 summarizes the GIXRD in-plane study of the layer stack. Fig. 19(a) shows a sketch of the reciprocal space of the hexagonal Si (111) surface system. The errors of the synchrotron measurements are in the last digit of the reciprocal space values and therefore omited.

Discussion of the <$11\bar{2}$> *azimuth:* The scan depicted in Fig. 19(b) is a scan along the $[h00]^{\mathrm{surf}}$ direction form h^{surf}=0 to h^{surf}=3.5 at an angle of incidence $\alpha = 0.6^\circ$ and l^{surf}=0.5. The scale has been calibrated in such a fashion that the Si $(22\bar{4})^{\mathrm{bulk}}$ Bragg peak exactly coincides with the $(300)^{\mathrm{surf}}$ coordinate. In this scan range, there is one Bragg peak expected for both the Ge and the Si, namely the $(22\bar{4})^{\mathrm{bulk}}$ peak at h^{surf}=3. The (1x1) surface unit cells create a sharp crystal truncation rod for Si (h^{surf}=1), and close to Si at lower reciprocal lattice units (r.l.u.) for Ge (h^{surf}=0.96). Those peaks are found and labeled accordingly. The only peak missing is the Si CTR expected at h^{surf}=2. This peak is very delta-peak-like due to the high crystalline perfection and interface sharpness of the Si wafer. As it is so sharp, the detector might have missed it due to the applied step width in the scan. There are four Pr_2O_3 Bragg peaks expected, namely the $(\overline{11}2)^{\mathrm{bulk}}$, the $(\overline{22}4)^{\mathrm{bulk}}$, the $(\overline{33}6)^{\mathrm{bulk}}$ and the $(\overline{44}8)^{\mathrm{bulk}}$ peaks. The assignment of the peaks is as shown in Fig. 19(b). The antiparallel indexing of the Pr_2O_3 peaks with respect to the Si peaks ac-

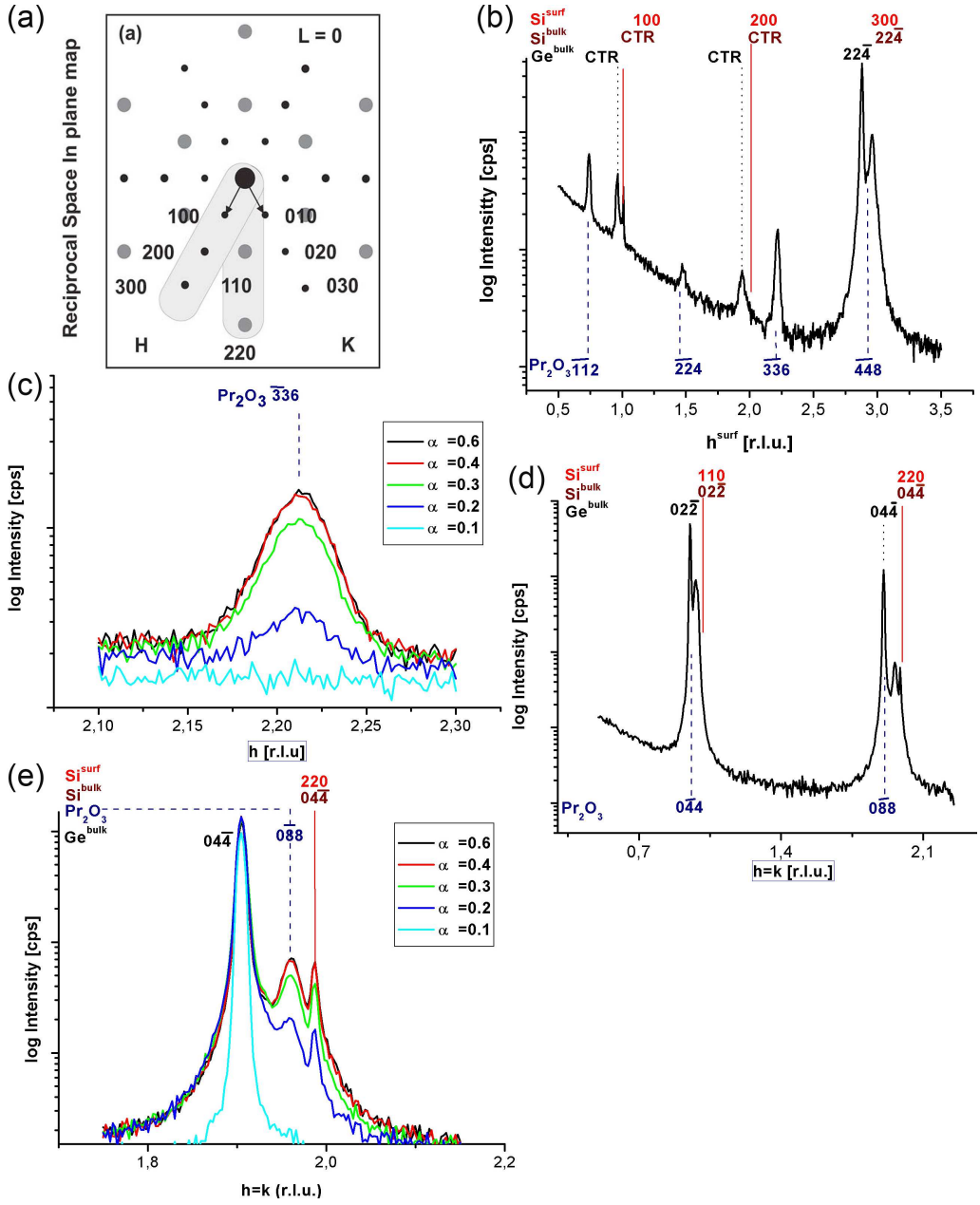

FIG. 19: GIXRD in-plane scans of the closed Ge layer sample. Different surface lattice directions, overview and high resolution scans to determine the azimuthal orientation of the Ge layer

counts for the exclusively type B grown oxide layer [19]. The parallel indexing for the Ge layer accounts for the type A stacking of the Ge. The overall decrease of the intensity with increasing h values is due to the polarisation factor in the Thomson scattering formula (A.5).

Fig. 19(c) reveals several important points. It shows a high resolution scan over the Pr_2O_3 $(\overline{3}\overline{3}6)^{bulk}$ Bragg peak at various incident angles. This demonstrates the advantage of GIXRD. At this peak, no disturbing intensity is diffracted by the Ge layer or the Si wafer, due to their different crystal symmetry in the unit cell. This enables a non-destructive study of the layer, even though it is buried below 86 nm of Ge. A lattice d-spacing of 1.504 Å can be calculated from the peak position of h^{surf}=2.212, which is 0.9% smaller than the expected bulk value. Therefore, the buried oxide is under compressive strain.

This is expected as it is grown on a semi-infinite large Si crystal whose in-plane lattice constant is 2.4% smaller than the one of Pr_2O_3. The in-plane domain size can be directly estimated from the full width at half maximum to be around 10 nm, indicating a high defect density that limits the amount of coherently scattering unit cells. The peak clearly vanishes with decreasing angles of incidence. This is a proof that the Ge layer on top is closed, even on a scale of cm^2, given by the large footprint of the x-ray beam in grazing incidence geometry. If the Ge layer was not closed, the oxide peak would be still visible (depending on the layer thickness), even for $\alpha = 0.1^\circ$, which is below the critical angle for total reflection on the Ge surface. The peak position does not change with the incidence angle, indicating a homogeneously strained oxide layer, as the attenuation length is decreased with a lower incidence angle.

Discussion of the <01$\bar{1}$> *azimuth:* An in-plane scan (Fig. 19(d)) along the h^{surf}=k^{surf} (which is the $[01\bar{1}]^{bulk}$ direction) showed no peaks except those around h^{surf}=k^{surf}=1 and h^{surf}=k^{surf}=2. For h^{surf}=k^{surf}=1 the Si peak is missing, but here again it is most probable that it was missed in this overview scan due to the detector step width. In Fig. 19(d), there are two more peaks with slightly smaller reciprocal lattice units than h^{surf}=1. At h^{surf}=k^{surf}=2, a three peak structure is seen; the reduced Si peak intensity might be again due to the sharpness of the peak. The peaks are labeled according to the theoretically expected values. A type A and type B stacking nomenclature applied for Ge and Pr_2O_3, respectively.

Fig. 19(e) shows a high resolution scan over the h^{surf}=k^{surf}=2 region at different angles of incidence. The diffraction signals can be assigned to the lattice planes as indicated in the figure. The lattice d-spacing of the Pr_2O_3 $(0\bar{8}8)^{bulk}$ lattice planes is calculated to be 0.973 Å from the measured peak position at h^{surf}=k^{surf}=1.973. This is about 1.3% smaller than the theoretically expected value of d=0.985 Å. The entire oxide layer is under compressive strain, most likely due to the 2.4 % smaller lattice constant of Si. It is reminded that the lattice mismatch of Ge and the oxide is 1.6%. This shows that the strain of the oxide buffer is not isotropic, i.e., it exhibits an anisotropy in the high symmetry directions, most probably a result of the tetragonal distortion of the oxide [43].

Here, it is shown again that the Ge layer is closed, as both the Si $(04\bar{4})^{bulk}$ as well as the Pr_2O_3 $(0\bar{8}8)^{bulk}$ are suppressed for angles below the critical angle of Ge. This behaviour is therefore in line with the expectation. From the same in plane scan, the Ge $(04\bar{4})$ lattice d-spacing is measured at h^{surf}=k^{surf}=1.918 and calculated to 1.001 Å. This is with 0.1% in line with the bulk value of 1.000 Å. This is very well within the limits of the measurement. The Ge layer can be assumed to be fully relaxed in average. From the FWHM of the peak, a first estimate of the domain size is calculated to be around 20 nm. The Ge layer is therefore defective and a further detailed investigation of the defects in the layer is neccessary, as discussed in the defect study in the following.

Out-of-Plane Measurements:

The type A orientation of the Ge and along with that the parallel indexing of the Ge Bragg peaks with respect to Si, which was assumed in the preceeding, can be confirmed in the vertical stacking orientation by out-of-plane scans, summarized in Fig. 20. Fig. 20(a) shows the $[0,1,l]^{surf}$ scan. The Kiesig fringes surrounding the Pr_2O_3 peaks indicate a very smooth oxide layer. From the distance of these Kiesig

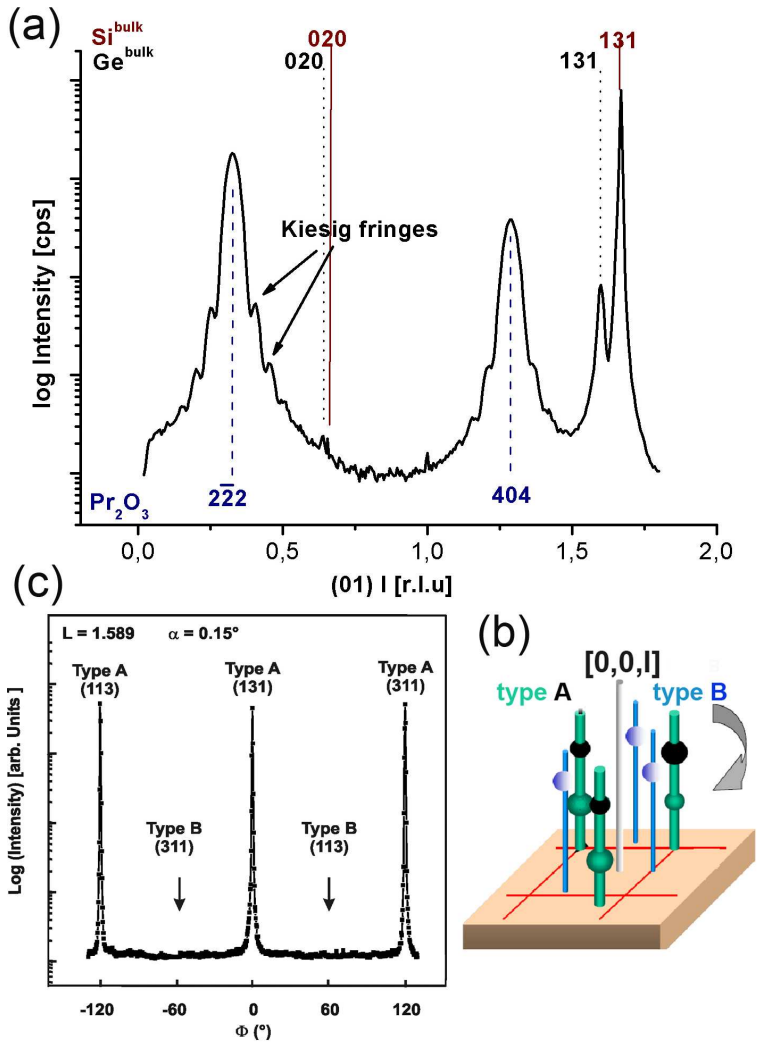

FIG. 20: GIXRD off-plane (out-of-plane) scans. (0,1,l) rod scan, model of the surface symmetry, and a ϕ scan over the Ge (131) spot.

fringes, the layer thickness is calculated to be 8 nm, which is in agreement with the layer thickness obtained from XRR. The $(131)^{bulk}$ reflection is the only expected reflection for Ge (111) as well as the Si (111) wafer. From the position of the Ge $(131)^{bulk}$ peak at l^{surf}= 1.599, the lattice d-spacing can be calculated to be 1.689 Å which is about 0.9% smaller than the bulk value of 1.705 Å. This can be explained by the fact that the measurement was performed for the $[0,1,l]^{surf}$ rod position of the Si lattice: A correct measurement for Ge must be performed on the $[0,0.96,l]^{surf}$ rod, to fully hit the Ge Bragg peak and extract the lattice parameters. Therefore, this Ge (131) peak position is simply too inaccurate to deduce the lattice d-spacings and in consequence the strain status. The Si and Ge $(020)^{bulk}$ Bragg peaks, which are in principle also located on the $[0,1,l]^{surf}$ rod, are forbidden. There are two expected Pr_2O_3 bragg peaks, namely the $(2\bar{2}2)^{bulk}$ and the $(040)^{bulk}$ peaks. The lack of intensity at $(0,1,l=\frac{2}{3})^{surf}$ unequivocally proves the exclusive type B orientation of the buried Pr_2O_3 layer beneath a closed Ge layer. If there was any type A oriented oxide, there would be the Pr_2O_3 type B $(040)^{bulk}$ Bragg peak observed at this position. To show that the Ge layer is mostly type A oriented, a scan under grazing incidence

must be repeated, as, in a bulk sensitive Φ scan, a type B oriented Ge $(1\bar{1}1)^{bulk}$ would overlap with the Pr_2O_3 $(2\bar{2}2)^{bulk}$ peak, and the same for the type B Ge $(202)^{bulk}$ and the Pr_2O_3 $(404)^{bulk}$ peaks. Another possibility is a surface sensitive Φ scan around the $[0,0,l]^{surf}$ rod on the Ge$(131)^{bulk}$ Bragg peak position. The Ge $(131)^{bulk}$ Bragg peak position is chosen, and scanned with varying h^{surf} and k^{surf} with $h^2+k^2=1$. There are, according to the threefold symmetry of the [111] space diagonals of the cubic diamond lattice, three Bragg peaks expected, i.e., the Ge type A $(131)^{bulk}$, the $(311)^{bulk}$, and the $(113)^{bulk}$ peaks at the surface coordinates $(01\frac{5}{3})^{surf}$, $(1\bar{1}\frac{5}{3})^{surf}$ and $(\bar{1}0\frac{5}{3})^{surf}$. A scheme of the out-of-plane symmetry of the Ge $(131)^{bulk}$ Bragg peaks is given in Fig. 20(b). The expected threefold symmetry for an exclusive type A stacking is depicted by the green rods on the surface. Twinned grains with type B stacking exhibit the same symmetry, which creates three additional peaks, shown as blue rods on the surface. In the presence of type B as well as type A stacked Ge, there would be a sixfold symmetry. In the case of no present twinning, the symmetry would only be threefold.

The actual Φ scan, Fig. 20(b), clearly shows a threefold symmetry under grazing incidence. There are three peaks detected with an angular distance of 120°. This indicates that the top Ge layers are exclusively type A oriented.

TEM-Study and Structure Model:

HRTEM images were collected to visualize this epitaxial relationship.[3] Fig. 21(a) clearly shows a closed Ge layer on top of the Si wafer on a large 500 nm scale. Fig. 21(b) shows a zoom down to a scale of 40 nm. The two flaws at the oxide / Ge interface are a result of the sample preparation for TEM.

Fig. 21(c) is a flawless HRTEM of the Ge / Pr_2O_3 / Si interface region, along a stacking sensitive $[1\bar{1}0]$ viewing direction in real space. The Si wafer is seen, with the Ge layer on top, and the oxide in between. The region marked as IF is an amorphous interfacial layer, created in the ex-situ transformation in Oxygen ambient pressure before Ge deposition [20]. The white arrows indicate the $(11\bar{1})$ surface normals of each layer, showing the rotation around the (111) surface normal by π for type A / B / A epitaxy. This can be seen by inspecting the stacking sequence of the (111) layers at the interfaces: First a stacking fault is introduced in the (111) stacking at the Pr_2O_3 / Si interface, and second a stacking fault is again incorporated at the Ge / Pr_2O_3 interface.

Fig. 21(d) shows a summary of the situation at the Ge / Pr_2O_3 / Si interface by a developed idealized atomic model (it has to be noted that the structure of Pr_2O_3 is idealized to be CaF_2 and not bixbyte). Furthermore, the lattice constants were adapted to the Si in plane d-spacing for reasons of illustration.

[3] All of the presented TEM and HRTEM images were provided by Dr. D. Geiger and Prof. Dr. H. Lichte. For contact see [44]

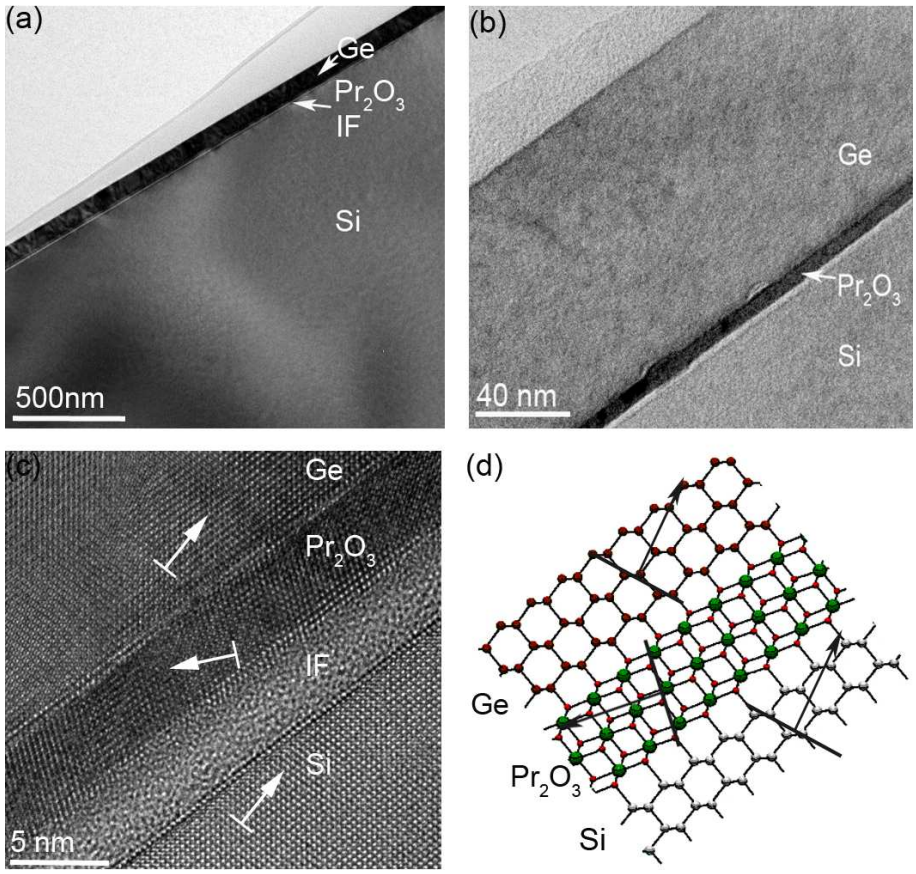

FIG. 21: TEM study of the closed Ge layer and the developed idealized atomic model along the $[1\bar{1}0]$ azimuth.

Key points of the epitaxial relationship:

In conclusion, the Ge layer is derived as closed and single crystalline with the listed properties.

– Specular $\theta - 2\theta$ Measurements:
  The growth texture and vertical growth were determined as

  $$Ge[111]\,||\,Pr_2O_3[111]\,||\,Si[111]$$

– In-Plane Measurements:
  The h and h=k scans allowed a full determination of the azimuthal in-plane orientation as

  $$Ge[11\bar{2}]\,||\,Pr_2O_3[\bar{1}\bar{1}2]\,||\,Si[11\bar{2}]$$

  Additionally, the [0,1,l] scan showed that the topmost part of the Ge layer is free of stacking twins.

– TEM-Study and Structure Model:
  The TEM study confirmed the anti-parallel orientation of the oxide with respect to Ge and Si, namely the type A / B / A heterostructure

3.2 Defects

The non-destructive in-plane XRD measurements showed an in-plane domain size of around 20 nm on a global scale. The destructive TEM images in addition indicate a high density of present defects that limit the long range order in the epi-Ge layer on a local scale (will be shown in the following). These facts make a detailed study of the defects necessary. In the following, first, a qualitative and quantitative analysis of the defects is given. Second, a thickness dependent study of the defect behaviour is discussed. Third, the defect characteristics under post-deposition treatment are given.

3.2.1 Identification of the Present Defects

A bulk sensitive Ge (111) pole figure measurement was carried out on the layer stack. The results of

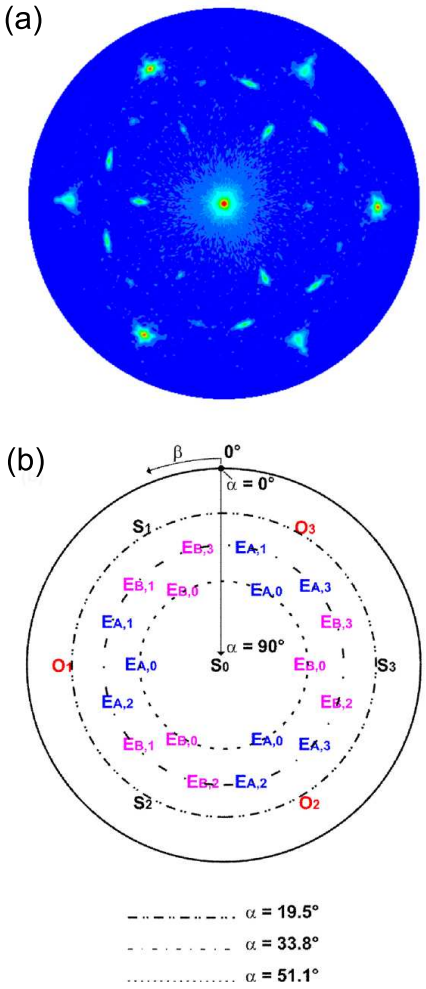

FIG. 22: Ge (111) pole figure of the closed layer system with the corresponding spot labels.

the pole figure measurements on the actual sample with a closed Ge layer are shown in Fig. 22(a). Each of the discussed intensities is labeled as explained, as shown in Fig. 22(b), with the corresponding diffractometer coordinates α and β. To define the $\beta = 0$ position, the direction of the incoming x-ray

beam was aligned along the $[11\bar{2}]$ direction of the Si wafer for $\beta = 0$. To define the $\alpha = 0$ position, the direction of the incoming beam was fixed perpendicular to the [111] direction for $\alpha = 0$. For the unexperienced reader, a detailed derivation of each spot is given in the following:

Fig. 23 is a sketch to simplify the understanding of the different diffraction spots in the pole-figure and

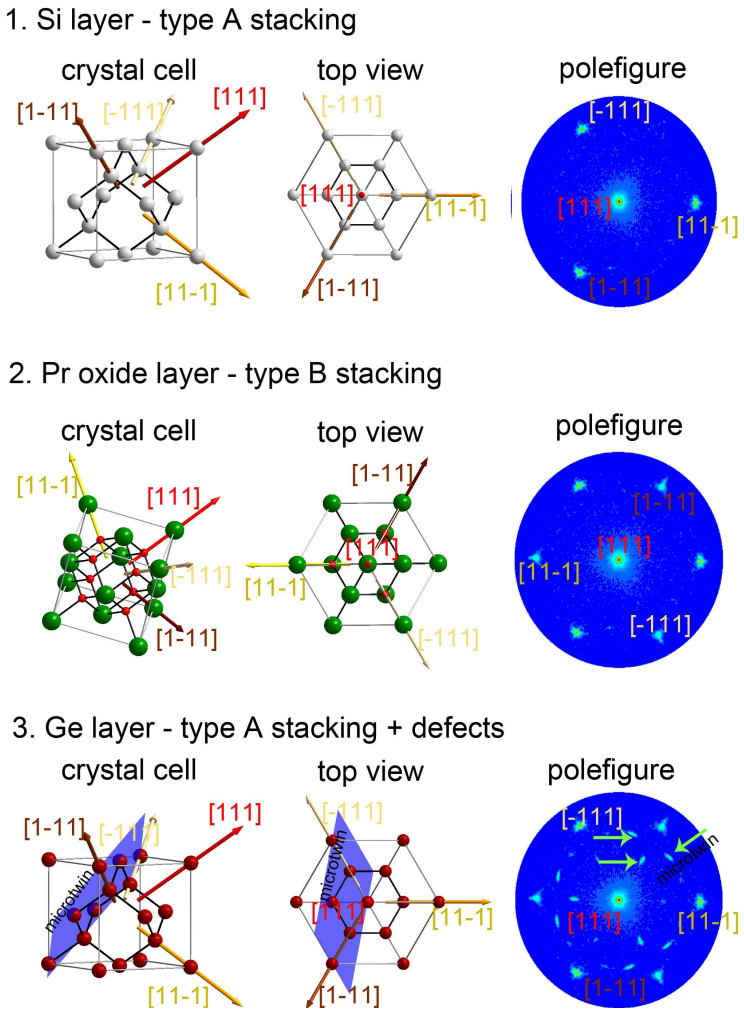

FIG. 23: Sketch of how the diffracted intensities in the pole figure are generated.

their origins. Starting with a plain Si (111) wafer, the well known crystal cell of the diamond lattice of Si and the [111], [11-1], [1-11], [-111] directions are highlighted by the arrows shown of the figure. The diffraction from these lattice planes is recorded in a Si / Ge (111) pole figure. The diffraction condition for the recording of the pole-figure is fixed to the {111} lattice plane d-spacing. As the Bragg angles for Ge (27.3) and Si (28.44) are so close to each other, the diffractometer is unable to resolve the two Bragg peaks at the selected in-plane parallel slit arrangement in the overview pole figure studies. The next images in Fig. 23.1 are the view on the (111) plane and the corresponding pole figure. Each of the given {111} planes diffracts at a certain angle α and β. Therefore, there are four spots originating from the Si wafer denoted as $S_{0,1,2,3}$ in the following.

Continuing to the oxide layer, again the crystal cell, the view on the (111) plane and the resulting pole

figure are given (Fig. 23(.2)). The oxide layer is turned by 180° around the [111] direction with respect to the Si layer, as derived as type A / B stacking. It is obvious that, e.g., the [1-11] direction of the oxide is antiparallel to the [1-11] direction in the Si layer, while the [111] direction of oxide and Si remain parallel. These lattice planes of the Pr_2O_3 contribute to the pole figure with four diffraction spots as well, hence forth denoted as $O_{0,1,2,3}$. Due to the parallelism of the [111] directions, the S_0 and the O_0 spot in the center coincide. The final layer on top is the Ge layer, depicted in Fig. 23(.3). In the type A / B / A stacking, the Ge layer {111} family net planes are again oriented parallel with respect to the Si wafer. Therefore, all the diffraction spots of a perfect single crystalline Ge layer coincide with the Si spots. Thus they have the same label as the Si $S_{0,1,2,3}$ spots. Additional features are not expected in a perfect heterostack. As they appear only after Ge deposition, they are due to defects in the Ge layer, which will be identified and investigated in the following, after a quantitative analysis of the unflawed layer Bragg peaks. The spots and corresponding lattice planes that are expected in the pole figure are summarized in table (1).

Spot	α[°]	β[°]	lattice plane Si	lattice plane Ge	lattice plane Pr_2O_3
S_0	90	0	(111)	(111)	(222)
S_1	19.5	30	$(\bar{1}11)$	$(\bar{1}11)$	
S_2	19.5	150	$(1\bar{1}1)$	$(1\bar{1}1)$	
S_3	19.5	270	$(11\bar{1})$	$(11\bar{1})$	
O_1	19.5	90			$(22\bar{2})$
O_2	19.5	210			$(\bar{2}22)$
O_3	19.5	330			$(2\bar{2}2)$

TAB. 1: Expected Bragg peaks from {111} family net planes

The presence of only the asserted material Bragg peaks in these spots can be proven by $\theta - 2\theta$ scans in each of the spots, especially the presence of type B Ge grains can be investigated by $\theta - 2\theta$ scans in the oxide (O_x) spots. Note that the scan over β at a fixed α value is nothing else but a ϕ scan as presented in Fig. 20(c), as $\beta = \phi$, with bulk sensitivity for the pole-figure. Fig. 24(a) shows a $\theta - 2\theta$ scan in the S_1 spot and a 180° turned scan in the O_2 spot. In the S_1 spot, there are two peaks, namely the Ge $(\bar{1}11)$ and the Si $(\bar{1}11)$ peak, at their theoretically expected positions of 27.3° and 28.44°, respectively. The existence of a Pr oxide peak at this spot cannot be fully excluded, as it would vanish between the two much stronger Si and Ge peaks. However, the off-plane scans unambiguously showed that the oxide is exclusively type B oriented (Fig. 20(c)). In the $\theta - 2\theta$ scans in the O_2 spot, there is, additionally to the Pr_2O_3 $(\bar{2}22)$ peak at 28.18°, a weak peak at the Ge position at 27.3° visible. This shows that there is a small fraction of Ge grains in type B orientation. By fitting Gauss curves to the spectra (not shown), the peak areas of the type B Ge and type A Ge are calculated and compared. The ratio of type B to type A oriented grains amounts to 0.5% for a Ge layer of 86 nm thickness. The Φ scan under grazing incidence showed, however, a threefold and not a sixfold symmetry, proving an exclusively type A oriented region within the attenuation length of the x-ray beam. Thus this exclusiveness can only be claimed for the topmost part of the Ge layer. This findings indicate that the type B 'twins' are located in the bottom part of the Ge layer, close to the oxide interface. Analogous to the Pr_2O_3 / Si interface, the electrostatic forces at the interface

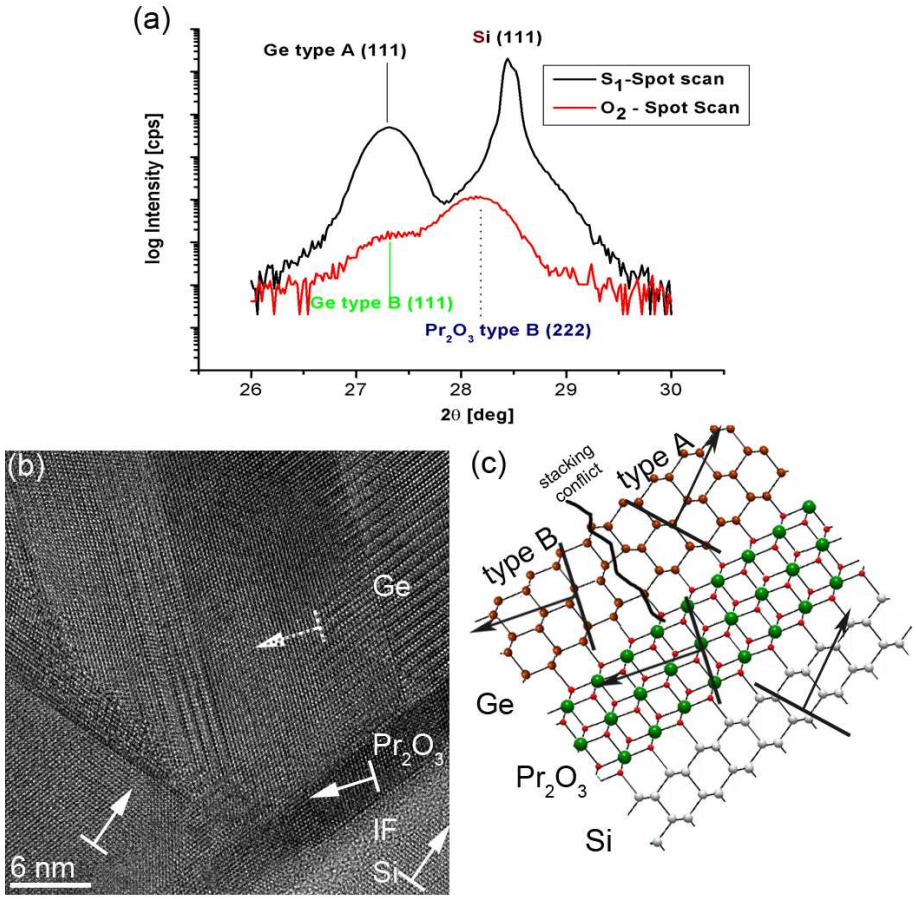

FIG. 24: Stacking twins: Large area diffraction information combined with real space TEM image of the defect in the Ge layer and the developed idealized atomic model along the <1$\bar{1}$0> azimuth.

make a local wurzite structure favorable over the cubic configuration, introducing the stacking fault at the interface. For Ge this type A configuration is 44 meV per Pr interface atom below the corresponding type B orientation. From the energetic point, of view the type B twinned Ge grains, surrounded by a type A Ge matrix, increase the energy of the entire system, due to the occurance of stacking conflicts in the Ge layer. Because of the energy minimization, the growth of the stacking conflicted grains with the layer thickness is not favored. The confinement of stacking twins to the interface-near region was also reported for a GaP on Si [58], and will be further corroborated in this study in the thickness dependent section. Fig. 24(b) shows a TEM image of such a stacking twin close to the interface along a <1$\bar{1}$0> stacking sensitive direction. The Si wafer can be seen in its type A stacking, on top of a thin interfacial layer due to the ex-situ annealing, the type B oriented Pr_2O_3 film and on top the Ge layer. The ($\bar{1}$11) surface normal of each layer is indicated by the white arrows. The Ge exhibits type B (dotted arrow) and type A (solid) grains. For those, it can be nicely seen that the stacking sequence continues from the oxide on to the Ge grains. For the type A Ge, the situation is the same as shown in the unflawed TEM image in Fig. 21. In between the type A and type B Ge there is some kind of flawed and strained stacking conflicted area. Fig. 24(c) shows the corresponding idealized atomistic model developed for this heterostack. Here, the ($\bar{1}$11) surface normals of each layer and grain are indicated by a black arrow.

Returning to the the pole figure, Fig. 22, there are not only the substrate and oxide spots at $\alpha = 19.5$, but there are more spots. In the derivation of the composition of the pole-figure it is stressed that no additional spots are expected from unflawed layers. The additional spots observed are denoted as $E_{A,B,0,1,2,3}$. It was already hinted that these features are due to crystalline defects in the Ge layer. The spots are in detail:

Spot	α[°]	β[°]	Spot	α[°]	β[°]
$E_{A,0}$	51	90	$E_{B,0}$	51	30
$E_{A,0}$	51	210	$E_{B,0}$	51	150
$E_{A,0}$	51	330	$E_{B,0}$	51	270
$E_{A,1}$	34	70	$E_{B,1}$	34	10
$E_{A,1}$	34	110	$E_{B,1}$	34	50
$E_{A,2}$	34	190	$E_{B,2}$	34	130
$E_{A,2}$	34	230	$E_{B,2}$	34	170
$E_{A,3}$	34	310	$E_{B,3}$	34	250
$E_{A,3}$	34	350	$E_{B,3}$	34	290

They seem to be dominated by a threefold symmetry as well. To understand their composition and symmetry, another sketch is given in Fig. 25. A $\theta - 2\theta$ Bragg scan over each of the spots (not shown) reveals that they have their maximum at θ=27.3°. As this corresponds to the Ge (111) Bragg angle, they are features generated only in the Ge layer. Keeping the threefold symmetry of the {111} net planes in mind, each of these features can be assigned to one of the Ge {111} spots. This should be clear, following the example of the Ge Bragg peak in the S_0 spot (red arrow in Fig. 25). In this spot the diffraction from all (111) lattice planes, namely from (111) planes in type A as well as type B Ge grains, coincides. The defects in those (111) planes must, of course, respect the same threefold out-of-plane symmetry as the unflawed planes. For the type A Ge: First of all, it is accompanied by three stonger peaks at α=51°, namely the $E_{A,0}$ peaks, highlighted by the red circles. This position at α=51° corresponds to an inclination of (90-51)°=39° with respect to the (111) surface normal. The strong $E_{A,0}$ peaks have a distance in β of 120°, corresponding exactly to the symmetry of the {111} net planes. For the type B Ge: The $E_{B,0}$ have the same symmetry, with a 180° turn with respect to the $E_{A,0}$ spots; they are highlighted by the green circles in Fig. 25. An analogous assignment can be made for all the other S_n and O_n spot, namely to every Ge Bragg peak in the diffraction spots. Drosd et al. reported the formation of microtwins, which are twin bands lying in one of the {111} planes [45]. Each of the diffraction signals can be assigned to a microtwin in one of the {111} planes. The planes in the twin band have a d-spacing equal to the Ge (111) d-spacing, inclined by 39° with respect to the (111) surface normal

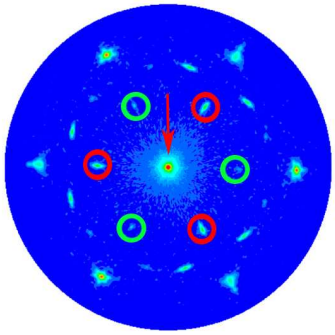

FIG. 25: Scetch to understand the symmetry of microtwin diffraction spots in the pole-figure.

of the heterostructure. The spots denoted by E_A belong to microtwins in the type A oriented Ge layer, while the spots denoted with E_B belong to microtwins in the type B oriented Ge grains. A close inspection of the spot shape reveals that the microtwin diffraction signals do not have a point-like shape, but rather a rod-like shape. This can be explained by a continuous transition of the lattice d-spacing and orientation of the (111) planes in the microtwin, caused by compressive and tensile stresses acting on the twin lamella. This was described in detail by our group in [46]. Fig. 26(a) shows a TEM image of

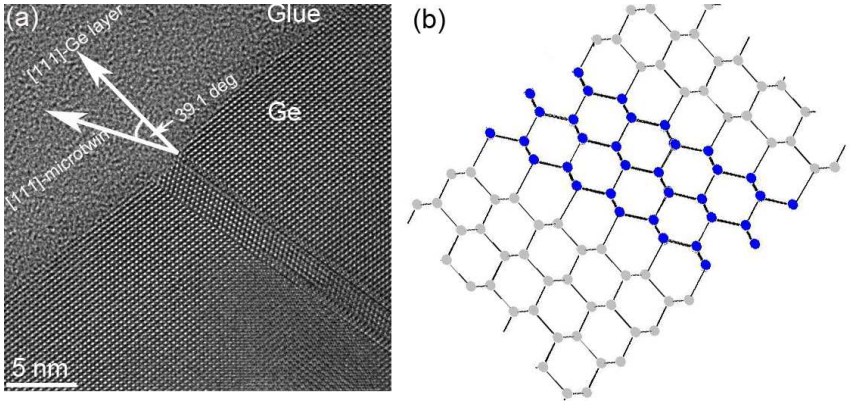

FIG. 26: Microtwins: TEM image and atomistic model imaged along a <1$\bar{1}$0> azimuth.

such a microtwin, imaged along a <1$\bar{1}$0> direction. The inclination of the (111) lattice planes in the twin band are obviously the same as the inclination of the diffraction spots in the pole figure (e.g., $E_{n,0}$ with respect to S_0), i.e., 39.1°. The white arrows indicate the (111) surface normals of the microtwin and the normal (111) surface normal. Fig. 26(b) shows the developed atomistic model, viewed along a <1$\bar{1}$0> azimuth. The Ge atoms in the microtwin are highlighted as blue for better visibility, surrounded by an unflawed Ge matrix (grey atoms). A quantitative analysis of the amount of the microtwins is much more complicated, as the intensities of the peaks in the pole figure are additionally a function of the tilt angle α, and go therefore beyond the scope of this thesis.

A reciprocal space map (RSM) was recorded around the Ge (111) peak (Fig. 27), also denoted as S_0 spot in the pole figure (Fig. 22). As mentioned before, in this spot, the diffraction from all three layers is present. The RSM axes are chosen with respect to fixed crystallographic orientations, namely the Si [111] (Q_z) and the Si [11$\bar{2}$] (Q_x) direction. The scale is given in units of the scattering vector, but could also be given in 2θ and θ. Therefore, the RSM is nothing but a contour plot of many θ scans for each of the 2θ values. For Q_x=0, the RSM would include only the specular θ - 2θ scan as given in deduction of the epitaxial relationship. In the RSM, there are several prominent spots. The bulk positions for the Si (111), Ge (111) and the Pr_2O_3 (222) Bragg peaks are indicated in Fig. 27. The Ge peak is, at its bulk value, surrounded by a wide halo, compared to the very sharp Si reflection. The Si is as sharp due to the high crystalline perfection of the wafer, while the Ge long range order is limited by defects, such as the ones discussed above. The Pr_2O_3 oxide peak intensity vanishes in the flanks of the Ge peak, due to its much smaller intensity as a consequence of its very limited thickness. The most striking feature in the RSM is the pronounced streak, inclined by 70° with respect to the Q_z (= Si [111]) direction, and

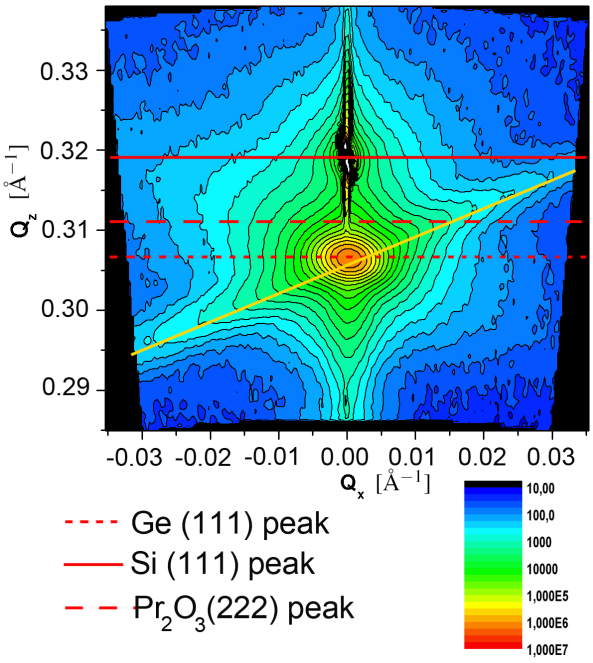

FIG. 27: RSM around the Ge (111) bragg peak. The bulk Q_z (=2θ) value of each material is indicated by the red lines. The streak in [11$\bar{1}$] direction is highlighted by the yellow line.

20° to the Q_x (=Si [11$\bar{2}$]) in-plane direction, highlighted by the yellow line. Correspondingly, the streak direction belongs to the surface normal direction of (11$\bar{1}$) planes. Two mechanisms can be assigned to this scattering in [11$\bar{1}$] direction. It is not unlikely that it is a superposition of both:

1. A crystal truncation rod created by the sharp interface with the microtwins in the type A Ge. They create a very sharp surface in the (11$\bar{1}$) planes. A close inspection of the TEM image (Fig. 26), shown for the microtwins, reveals the sharp surface created by the defect.

2. Scattering by the two-dimensional lattice plane created by extrinsic and intrisic stacking faults, which lie in the (11$\bar{1}$) slip system, as it has been shown for Si(111) layers [47, 48].

The strain fields surrounding the defects additionally create diffuse scattering around the Ge Bragg peak, as can be seen as a wide halo surrounding the Ge peak in comparison with the sharp Si peak.

3.2.2 Distribution of the Investigated Defects

In the following, a short study on the thickness dependence of the investigated defects is given. The defects regarded in this investigation are microtwins and stacking twins. All the grown samples were deposited at the closed layer conditions, discussed in the development of the growth recipe. The different thickness of the layers was obtained by changing only the deposition time. Five samples were prepared:

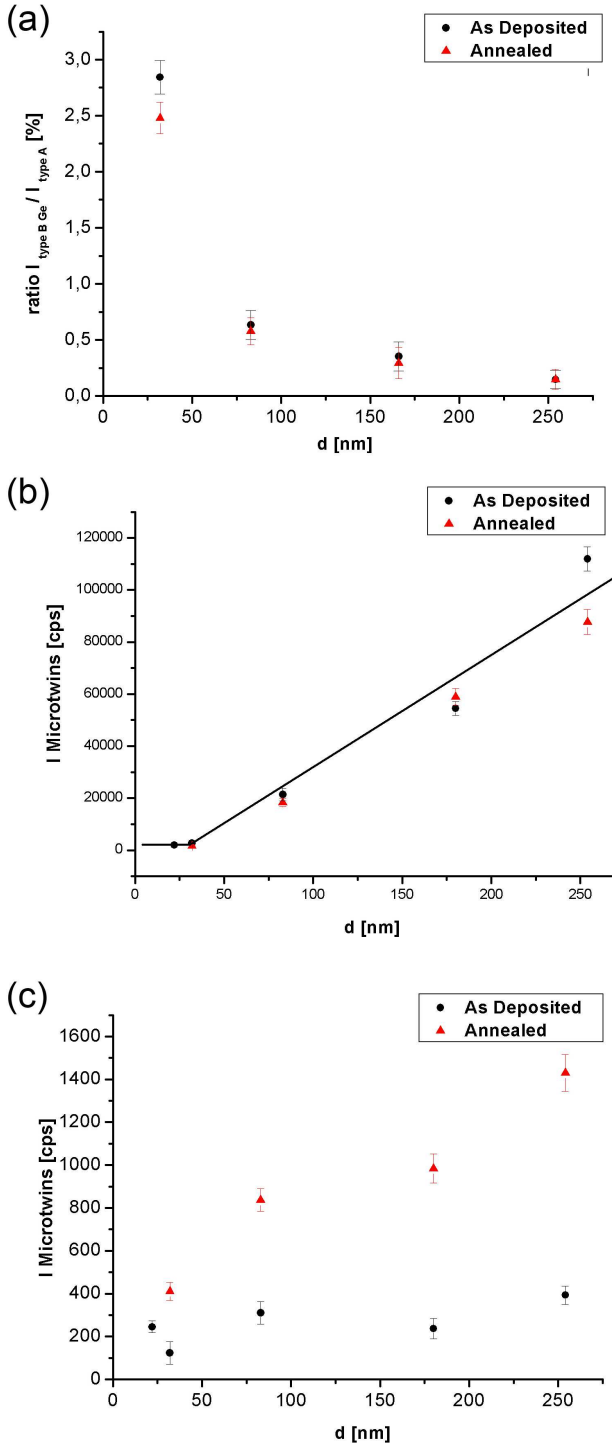

FIG. 28: Thickness dependent study of the stacking twins (a), the microtwins in the type A Ge layer (b), and the microtwins in type B Ge grains (c) on the as deposited Ge layers (black), and annealed layers (red).

Sample	thickness [nm]	Pr_2O_3 buffer thickness [nm]
1	22	12
2	32	9
3	86	10
4	180	8
5	254	9

The ratio of type B to type A oriented Ge was evaluated by $\theta - 2\theta$ scans in the O_1 and S_1 spots of the pole figures of each sample, as described above. The results can be seen in Fig. 28(a). The ratio decreases with the layer thickness. The decrease is evident, thus the stacking twins are found in Ge layer parts closer to the oxide interface, as indicated by the GIXRD study and the behaviour of the microtwins with increasing layer thickness (see below). The actual functional dependence is more complicated, as several effects superimpose here. The parameters are: the incomming intensity, the scattering intensity of the type A oriented Ge layer, which is an increasing function with the layer thickness, the scattered intensity of the type B oriented grains, and the attenuation with a decreasing function of the layer thickness. The type B grains are located closer to the interface and thus the attenuation increases with increasing layer thickness, and therefore the recorded signal decreases.

To get an idea about the thickness dependence of the microtwins, pole figures measurements were carried out for each of the samples under exactly the same acquiring conditions (slits, geometry, anode voltage and current, ...). The absolute intensities of the microtwin spots in the type A oriented Ge ($E_{A,0}$) and the microtwin spots in the type B oriented Ge ($E_{B,0}$) were averaged and plotted over the layer thickness, as can be seen in Fig. 28(b) and Fig. 28(c), respectively. For the microtwins in the type A oriented Ge there is a plateau of a minimum intensity for the microtwins at very low layer thicknesses (d < 35 nm). For layer thicknesses above 35 nm, the intensity increases linearily with the layer thickness. The functional dependence is I=2200 cps for d < 35 nm, and I=-17000 + 480 $\frac{[cps]}{nm}\cdot$ d. The relative errors amount to $\approx$ 5%, and thus do not influence the qualitative discussion. The minimum intensity, i.e., the visible plateau, might be explained by a certain amount of microtwins that are introduced in the Ge crystal, to reduce the misfit induced strain. The microtwins are also discussed to compensate for height steps in the atomic range on the oxide / Ge interface [43]. For the linear increase in the intensity, there are two possible explanations.

Firstly, the microtwins created in the bottom part of the layer, are progressing through the entire layer, almost regardless of its thickness. Secondly, they might stop somewhere in the crystal and the density of microtwins increases with the layer thickness. From just the intensity of the Bragg reflections, neither interpretation can be favoured, nor ruled out. A comparison of RSMs of all samples and the comparison of the streak width due to the microtwins in $[11\bar{1}]$ direction could unravel the problem: If the microtwins progress through the entire layer, the inner defect long range order will be higher and the streak width will be smaller. To exclude the Ge layer effect, a RSM around a forbidden Bragg peak is necessary and is currently under investigation. Fig. 28(c) shows the plot of the averaged microtwin intensities in the type B oriented Ge. The first obvious observation is that the intensities are much smaller than for the microtwins in the type A oriented Ge. Additionally, the intensity does not increase with the layer thickness. The intensities seem to be rather scattered around the value of 100 to 350 counts per second (cps). The amount of microtwins in type B Ge grains is, however, increased compared to the amount of microtwins in the type A Ge layers (about one order of magnitude). This higher defect density in the type B Ge grains indicates the high strain state, caused by the surrounding Ge type A matrix. The ratio of type B to type A oriented Ge was found to be around 0.5% for a layer thickness around 83 nm. It is logical that this type of microtwins only forms in a type B oriented Ge matrix, and not in an type A

oriented matrix. The GIXRD study indicated that the topmost Ge layer is free of stacking twins. This is additionally supported by the behaviour of the microtwins in type B Ge: As the type B Ge domains do not progress through the entire layer, no measure of the corresponding microtwin intensity with Ge layer thickness is found.

3.2.3 Defect Treatment

This study has the goal to reduce the defect density in the layer to achive a density that allows for the aspired technological applications.
The samples used for the thickness dependend study were reintroduced into the UHV and degased at 250°C for 30 min. After that, each of the samples is heated to 825°C at a rate < 2° per second. For 30 min the temperature is kept constant and then cooled down to room temperature again at a rate < 2° per second. The RHEED pattern changes from initially very diffuse to the streaky pattern, revealing the same Ge surface diffraction pattern as observed at the end of Ge deposition. Therefore, the Ge layers do not break up. XRR measurements of each annealed layer confirm that the layers have the same thickness and the same surface roughness as before the annealing of around 1 nm. The base pressure remains below 10^{-10} mbar at all times during the annealing. After the retrieval from the MBE system, the XRD measurements are repeated under the same conditions as for the thickness dependent study above. The influence of the annealing on the different types of defects found in the layer is:

- **Stacking twins:**
  The results are displayed in Fig. 28 as red triangles. Fig. 28(a) displays the ratio of type B Ge intensity to type A Ge intensity for the annealed samples as well. The functional dependence, namely the type B / A ratio decrease as a function of the layer thickness, is not changed. However, the type B / A ratio decrease for the annealed samples is evident. The improvement is strongest for the thinnest sample, and weakest for the the thickest sample. In Fig. (29a), Bragg scans in the substrate spot S_1 for both the as deposited and the annealed sample with a layer thickness of 86 nm are depicted. The Ge reflection has increased in intensity after annealing, while the Si reflection is unchanged. This is the case for all Ge peaks of all annealed samples (not shown). Fig. 29(b) shows a Φ scan over the S_1 spot at the Ge Bragg angle. The Φ scans in the same spot at the Si Bragg angle are shown as well for reference. At this tilt (70.5°), a Phi scan is almost an in plane θ scan revealing information about the in-plane mosaicity. Firstly, the Ge peaks are much broader than the Si peaks, as it is expected due to the decreased in-plane domain size, induced by the higher defect density. After the annealing, the Ge Bragg peaks become much sharper. This indicates a reduction of the in-plane mosaicity of the Ge layer, i.e., more Ge unit cells scatter coherently. This also explains the increase in the Ge Bragg peaks in Fig. 29(a). In conclusion, the type A Ge layer quality is improved. This is true for the type B Ge as well, but the effect is much smaller for the type B Ge grains (not shown). Thus the reduction of the type B/A ratio in Fig. 28(a) for the annealed samples can be explained mostly by the reduction of the type A Ge layer mosaicity.

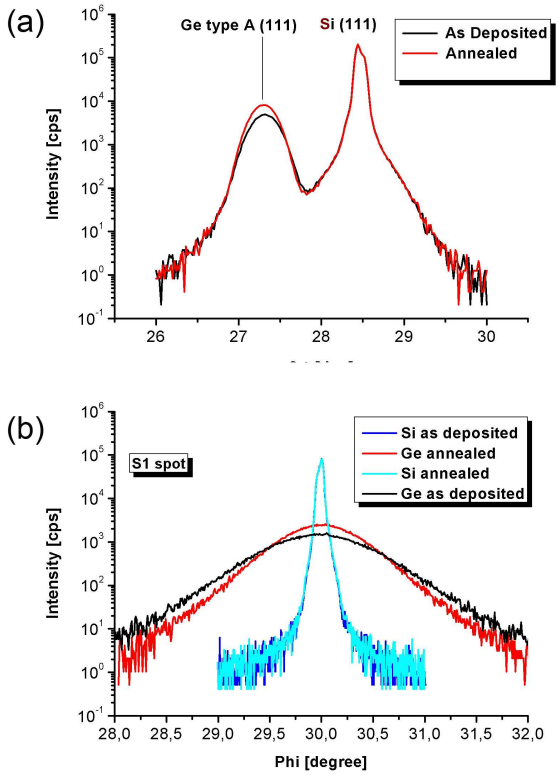

FIG. 29: $\theta - 2\theta$ scan and Φ scan over the S_1 spot, as deposited and after annealing.

– **Microtwins:**

Type A: The linear increase that has been corroborated for the intensity of the microtwins in the initial layer persits; as shown in Fig. 28(b), the red triangles apparantly follow the same functional dependence as the samples before deposition. The decrease of the intensity for the thickest layer is inconclusive and requires further studies to be confirmed.

Type B: The intensity of the microtwins in the type B oriented Ge grains seems to be not as scattered as for the as deposited sample; the intensities (red triangles) in Fig. 28(c) seem to linearly increase with the layer thickness. The intensity is even increased with respect to the pre-annealing status. Here, a linear increase of the intensity with the thickness is apparent.

A quantitative reduction of microtwins in the type A Ge layer cannot be deduced from this data. For the microtwins in the type B Ge, the intensity even increases. This might be a strain relaxation mechanism in the type B Ge grains that are undoubtedly in a strained state in the type A Ge matrix.

– **Stacking faults**:

The RSM measurement around the Ge (111) Bragg peak as shown for the as deposited sample in Fig. 27 was repeated for the annealed samples. Fig. 30 shows the results of the line scans indicated by the yellow line in Fig. 27 on the 86 nm Ge sample. The recorded intensity in counts per second is plotted over the scattering vector in Å^{-1}. The line scan becomes sharper. This means the width of the CTR and the diffuse scattering is reduced. Thus, the defect density along the $(11\bar{1})$ slip planes is reduced by this UHV high temperature annealing. There are two possible interpretations: The microtwin density is reduced for the annealed samples, or the number of stacking faults is reduced. As it has been shown, the reduction of the microtwins is inconclusive, meaning that looking at the microtwin intensity for the 86 nm Ge sample, for which this line scan in the RSM is shown, there is no real reduction. Subsequently, the reduction in the defect density cannot be caused by a reduction of the microtwins, but must be a result of the reduction of stacking faults.

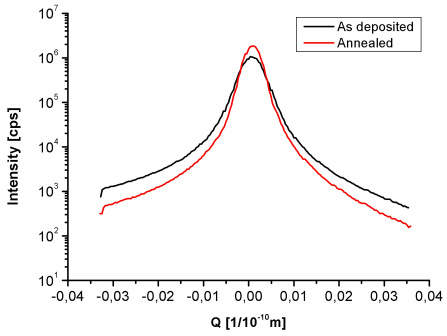

FIG. 30: RSM line scan along the $[11\bar{1}]$ streak, before and after the annealing.

4 Summary and Outlook

4.1 Growth

The first task of this thesis was the development of closed single crystalline Ge layers on the Pr_2O_3 (111) / Si (111) support system. This was successfully achieved by developing a growth recipe, consisting of two steps, namely

1. single crystal seed deposition at 600°C, and
2. smoothening out of the Ge layer at 0.8 nm / min of flux and at 300°C,

resulting in closed single crystalline Ge layers. The growth is summarized in the pictograph of Fig. 31: The initial Volmer-Weber growth front is smoothed in the continued deposition process by meeting the

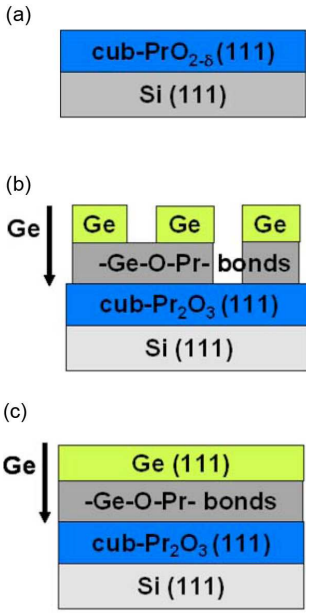

FIG. 31: The development of the Ge layer growth with deposition time. From the initial Volmer-Weber growth to the final smooth layer.

appropriate kinetic requirements. In the initial Ge deposition, the cubic-PrO_2 buffer is reduced to Pr_2O_3 by the formation and re-evaporation of GeO_2. The behaviour of the Ge deposit could be understood in terms of the thermodynamics and kinetics of growth theory. First, during the high temperature deposition step the heteroepitaxial growth follows a Volmer-Weber mode, driven by the functional dependence of the chemical potential. Second, the growth front is smoothed out with increasing layer thickness during the low temperature deposition step, following the expected crystal growth behaviour, as the influence of the oxide interface is weak, and the Ge layer is fully relaxed. Here, the system relaxes into the facet with the lowest surface energy: The (111) surface. This results in the final closed and smooth layer.

4.2 Structure

The substantial findings of the investigation of the structure of the layer system are:

- Specular $\theta - 2\theta$ Measurements:
  The vertical growth was determined as parallel for all three layers in the (111) surface normal direction. The relative layer orientation could be determined as:

  $$Ge[111] \,||\, Pr_2O_3[111] \,||\, Si[111]$$

- In-plane and out-of-plane Measurements:
  The azimuthal film orientation of Ge is parallel to Si and anti-parallel to Pr_2O_3. A type A / type B / type A heterostructure of the Ge (111) / Pr_2O_3 (111) / Si (111) stack was derived. The relative layer orientations were determined as:

  $$Ge[11\bar{2}] \,||\, Pr_2O_3[\bar{1}\bar{1}2] \,||\, Si[11\bar{2}]$$

  Additionally, the [0,1,l] scan showed that the topmost part of the Ge layer is free of stacking twins. The peak positions of Pr_2O_3 indicate a compressive strain over the entire layer. The Ge deposit on top is fully relaxed.

- TEM-Study and Structure Model:
  The TEM study confirmed the anti-parallel orientation of the oxide with respect to Ge and Si, namely the type A / B / A heterostructure.

4.2.1 Defects

The second task of this thesis was to identify the grown-in defects and to investigate their behaviour. The domain size in the Ge layer was determined to be 20 nm. The main defect mechanisms at work could be identified as

1. stacking twins,
2. microtwins,
3. stacking faults,

as summarized in Fig. 32.

The thickness dependence was investigated and revealed a threading behaviour of microtwins and stacking faults, while the confinement of the stacking twins to the Ge / Pr_2O_3 interface was confirmed.
The results of the treatment of the defects by high temperature UHV annealing indicates a reduction of stacking faults and an unaltered density of stacking twins as well as microtwins.

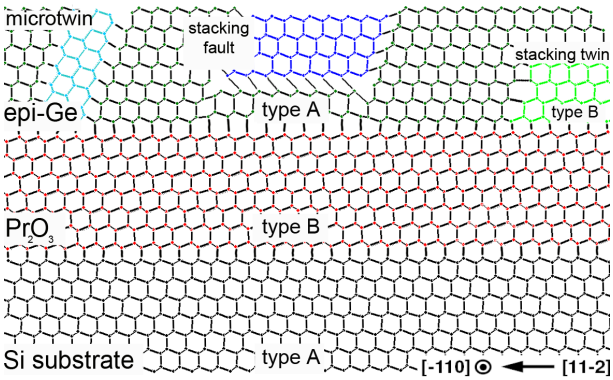

FIG. 32: Summary of the epitaxial relationship and investigated defects in the Ge layer.

4.3 Outlook

1. **From Material Science to Manufacturing Science**

   MBE as a growth technique is, as mentioned, only a proof-of-principle technique for fundamental research. A main point of criticism is the very limited throughput of samples due to UHV conditions. To make the system relevant for Si microelectronics and photovoltaics, which are mass markets, manufacturing science must be considered in the future. Therefore, the material system will be introduced to CVD (Chemical Vapour Deposition) as a mass production compatible growth technique. The kinetics of the growth play an important role in the determination of the growth mode. In CVD, the deposition usually takes place via a carrier gas and a precursor, in the case of Ge this is typically Argon (Ar) and Germane (GeH_4). As suggested in the literature, the Hydrogen in the precursor can act as an active diffusion barrier on the surface and might thereby reduce the formation of islands and thus change the growth mode [49]. First results of CVD grown Ge layers are very promising, even though the growth mode cannot be monitored in-situ in the AIXTRON TRICENT CVD reactor at the IHP. Along with the kinetics, the thermodynamics play an important role: The introduction of surfactants into the growth process might change the surface energies and interface reaction, possibly even the growth mode.

   Results of secondary ion mass spectoscropy additionally reveal that the oxide layer acts as a diffusion barrier between Si and Ge. No Si is found in the Ge layer, not even in the range of parts per billion. This is, in contrast to Ge growth on graded SiGe buffers to compensate the strain gradually, a major advantage of the buffer oxide approach.

   The evaluation of the contribution of this work to technological advance will be provided by the results of ongoing experiments of the integration of III-V semiconductors on the Ge layers for the application in photovoltaics. However, a real impact of technological relevance will only be for Ge layers with a defect density $< 10^{-5}$ per cm^2, which was not yet achieved here.

2. **Defect Engineering**

   Future investigations of the defects will require the more complicated quantification of the amount of microtwins with respect to the unflawed Ge. The thickness dependent study of the scattering

in $\{11\bar{1}\}$ slip planes will have to be carried out at a forbidden Bragg reflex, and is thus a task for future synchrotron studies, as laboratory equipment does not provide the necessary intensity for such a study. Such a study will reveal the thickness dependent behaviour of the stacking faults, and corroborate the threading behaviour of the microtwins.

More advanced defect reduction and engineering approaches are proposed for the reduction of the defect density in the Ge layer, such as multiple layer growth or epitaxial lateral overgrowth, which is, for instance, the state-of-the-art technique for the production of GaN based blue lasers today.

A Kinematical Diffraction

This appendix follows the standard literature on x-ray diffraction. For a thorough treatment, reference should be made [33, 50, 36, 51].

There are two types of scattering of x-rays: Unmodified and Compton modified scattering. The latter is based on the Compton effect, which describes a transfer of momentum from the x-ray photon to the electron in the electric field of an atomic nucleus. In classical scattering, only the unmodified scattering is included. The calculation of the scattered intensities with classical theory is therefore containing approximations, but nevertheless leads to good results, which are comparable with the calculations from the correct wave mechanical treatment. The polarization is even given correctly by the classical treatment: Electrons in an oscillating electrical field follow this oscillation and are thus subjected to constant accelleration. According to electromagnetic theory by Maxwell, radiation is emitted at a frequency equal to the primary oscillation. All of the following examples can be considered as weak, and, importantly, single scattering. This limit is known as the *kinematical diffraction* theory.

A.1 Scattering by one Electron

A single electron, subjected to an unpolarized primary beam, at the origin of the coordinate system is considered (Fig. 33). The intensity of the scattered radiation at the point P is to be derived. The electric field of the primary beam is E_0 and can be displayed in its componends:

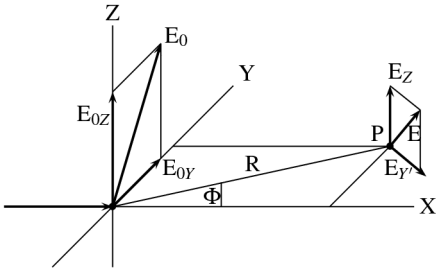

FIG. 33: Classical scattering [33].

$$\varepsilon_{0Y} = E_{0Y}\sin(2\pi\nu t), \qquad \varepsilon_{0Z} = E_{0Z}\sin(2\pi\nu t), \qquad \text{(A.1)}$$

The force f_Y on the electron due to the electric field in Y-direction causes an accelleration

$$a_Y = \frac{f_Y}{m} = \frac{eE_{0Y}}{m}\sin(2\pi\nu t), \qquad \text{(A.2)}$$

with e and m the electrons charge and mass, respectively. The electric field of the emitted radiation due to this acceleration is given by

$$\varepsilon = \frac{ea\sin\alpha}{c^2 R} \qquad \text{(A.3)}$$

with c the speed of light in vacuum, R the distance from the electron to the point of observation P, and α the angle of E_{0Y} and R (see Fig. 33). In the depicted case E_{0Y} is parallel a, $\rightarrow \sin\alpha = \cos\phi$ resulting in the field of the emitted radiation at P

$$\varepsilon_{Y'} = \frac{e^2 E_{0Y}}{mc^2 R}\sin(2\pi\nu t)\cos(\phi) \qquad \text{(A.4)}$$

or with $\varepsilon_{Y'} = E_{Y'} \sin 2\pi\nu t$, in terms of an amplitude:

$$E_{Y'} = \frac{e^2 E_{0Y}}{mc^2 R} \cos(\phi),$$

The analogue calculation for the Z-direction and the appropriate averaging of the squares of the electric fields,

$$\langle E_{0Y}^2 \rangle + \langle E_{0Z}^2 \rangle = \langle E_0^2 \rangle \qquad \text{and}$$
$$\langle E_{0Y}^2 \rangle = \langle E_{0Z}^2 \rangle = \tfrac{1}{2} \langle E_0^2 \rangle,$$

yields to the intensity of the classical scattering at P:

$$I = I_0 \frac{e^4}{m^2 c^4 R^2} \left(\frac{1 + \cos^2 \phi}{2} \right). \tag{A.5}$$

This is also referred to as the *Thomson Scattering* equation. The latter part in parenthesis is also called the *polarization factor*.

A.2 Scattering by an Atom

Consider the setup shown in Fig. 34: A primary beam with amplitude E_0, in the direction of the unity wavevector $\vec{s_0}$, is incident on the atom positioned at O, and with the electron at $\vec{r_n}$. Scattering is observed at point P. Using equation (A.4), the field of the electron at $\vec{r_n}$ at the position P is

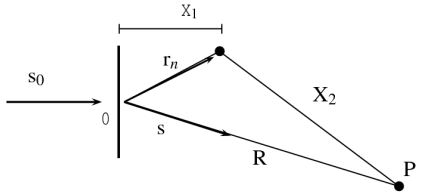

FIG. 34: Scattering from one atom [33].

$$\varepsilon_n = \frac{E_0 e^2}{mc^2 X_2} \cos\left(2\pi\nu t - \frac{2\pi}{\lambda}(X_1 + X_2) \right),$$

with the distances X_1, X_2 as seen in Fig. 34. Subsequently the contribution of an integer number of n electrons, positioned at $\vec{r_n}$ to the field at P reads

$$\varepsilon = \frac{E_0 e^2}{mc^2 R} e^{2\pi i[\nu t - (R/\lambda)]} \sum_n e^{(2\pi i/\lambda)(\vec{s} - \vec{s_0}) \cdot \vec{r_n}},$$

using $X_1 + X_2 \to \vec{r_n} \cdot \vec{s_0} + R - \vec{r_n} \cdot \vec{s} = R - (\vec{s} - \vec{s_0}) \cdot \vec{r_n}$ for the phase and $X_2 \to R$ in the plane wave approximation. As the electrons are not localized on discrete $\vec{r_n}$, one needs rather to integrate over the charge density distrubution ρdV. The electric field of the scattered beam due to the electrons in the atom is then:

$$\varepsilon_e = \frac{E_0 e^2}{mc^2 R} e^{2\pi i[\nu t - (R/\lambda)]} \int e^{(2\pi i/\lambda)(\vec{s} - \vec{s_0}) \cdot \vec{r}} \rho \, dV, \tag{A.6}$$

with the scattering factor per electron

$$f_e = \int e^{(2\pi i/\lambda)(\vec{s}-\vec{s_0})\cdot\vec{r}}\rho dV, \tag{A.7}$$

which is also called the *atomic scattering factor* and expresses the unmodified scattering per atom in electron units.

A.3 Scattering from a Small Crystal

Consider the situation displayed in Fig. 35. The electric field of the primary beam is E_0, the crystal origin is located at O, the observer at P, in the direction of the unit vector $\vec{s}$. The atom n in a unit cell is located at $\vec{R}_m^n = m_1\vec{a_1} + m_2\vec{a_2} + m_3\vec{a_3} + \vec{r_n}$. One condition that will be removed is that the primary beam is polarized with the electric field perpendicular to the scattering plane. Again, the plane wave approximation is used as the crystal is small compared to the distance between crystal and observer (R). Using equation (A.6) the electric field at P due to unmodified scattering from one atom is:

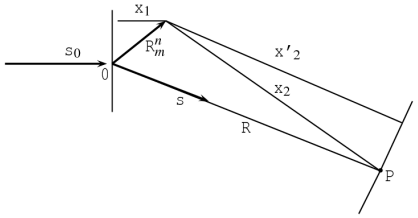

FIG. 35: Scattering from a small crystal [33].

$$\varepsilon_P = \frac{E_0 e^2}{mc^2 R} f_n \cos[2\pi\nu t - \frac{2\pi}{\lambda}(x_1 + x_2)]. \tag{A.8}$$

As the crystal size is negligible, $(x_1 + x_2) \to (x_1 + x_2')$. The electric field at P thus becomes

$$\varepsilon_P = \frac{E_0 e^2}{mc^2 R} f_n e^{i[2\pi\nu t - (2\pi/\lambda)(R - (\vec{s}-\vec{s_0})\cdot(m_1\vec{a_1} + m_2\vec{a_2} + m_3\vec{a_3} + \vec{r_n}))]}, \tag{A.9}$$

To gain the total field at P due to all atoms in the unit cell and all unit cells in the crystal, one needs to sum over n and $m_1 m_2 m_3$. The summation over the n atoms in the unit cell depends on the positions $\vec{r_n}$ and is accordingly a structure characteristic called the *structure factor*

$$F = \sum_n f_n e^{(2\pi i/\lambda)(\vec{s}-\vec{s_0})\cdot\vec{r_n}}, \tag{A.10}$$

Assuming a parallelepiped-shaped crystal with edges $N_1 a_1, N_2 a_2, N_3 a_3$, the total electric field at point P is:

$$\varepsilon_P = \frac{E_0 e^2}{mc^2 R} F e^{2\pi i[\nu t - (R/\lambda)]} \sum_n f_n e^{(2\pi i/\lambda)(\vec{s}-\vec{s_0})\cdot\vec{r_n}} \sum_{m_1=0}^{N_1-1} e^{(2\pi i/\lambda)(\vec{s}-\vec{s_0})\cdot m_1\vec{a_1}} \sum_{m_2=0}^{N_2-1} e^{(2\pi i/\lambda)(\vec{s}-\vec{s_0})\cdot m_2\vec{a_2}} \times \\ \times \sum_{m_3=0}^{N_3-1} e^{(2\pi i/\lambda)(\vec{s}-\vec{s_0})\cdot m_3\vec{a_3}}, \tag{A.11}$$

This can be simplified as the summations exhibit the form of geometric progressions:

$$\varepsilon_P = \frac{E_0 e^2}{mc^2 R} e^{2\pi i[\nu t-(R/\lambda)]} F \frac{e^{(2\pi i/\lambda)(\vec{s}-\vec{s_0})\cdot N_1\vec{a_1}}-1}{e^{(2\pi i/\lambda)(\vec{s}-\vec{s_0})\cdot\vec{a_1}}-1} \frac{e^{(2\pi i/\lambda)(\vec{s}-\vec{s_0})\cdot N_2\vec{a_2}}-1}{e^{(2\pi i/\lambda)(\vec{s}-\vec{s_0})\cdot\vec{a_2}}-1} \frac{e^{(2\pi i/\lambda)(\vec{s}-\vec{s_0})\cdot N_3\vec{a_3}}-1}{e^{(2\pi i/\lambda)(\vec{s}-\vec{s_0})\cdot\vec{a_3}}-1}, \quad \text{(A.12)}$$

As the intensity is the observable quantity, the square of the electric field is to be derived:

$$\varepsilon_P\varepsilon_P^* = \frac{E_0^2 e^4}{m^2c^4R^2} F^2 \frac{\sin^2[(\pi/\lambda)(\vec{s}-\vec{s_0})\cdot N_1\vec{a_1}]}{\sin^2[(\pi/\lambda)(\vec{s}-\vec{s_0})\cdot\vec{a_1}]} \frac{\sin^2[(\pi/\lambda)(\vec{s}-\vec{s_0})\cdot N_2\vec{a_2}]}{\sin^2[(\pi/\lambda)(\vec{s}-\vec{s_0})\cdot\vec{a_2}]} \frac{\sin^2[(\pi/\lambda)(\vec{s}-\vec{s_0})\cdot N_3\vec{a_3}]}{\sin^2[(\pi/\lambda)(\vec{s}-\vec{s_0})\cdot\vec{a_3}]},$$

using $I = E^2 c/8\pi$ and assuming an unpolarized beam, spacial averaging as carried out in the previous section yields to:

$$I_p = I_e F^2 \frac{\sin^2[(\pi/\lambda)(\vec{s}-\vec{s_0})\cdot N_1\vec{a_1}]}{\sin^2[(\pi/\lambda)(\vec{s}-\vec{s_0})\cdot\vec{a_1}]} \frac{\sin^2[(\pi/\lambda)(\vec{s}-\vec{s_0})\cdot N_2\vec{a_2}]}{\sin^2[(\pi/\lambda)(\vec{s}-\vec{s_0})\cdot\vec{a_2}]} \frac{\sin^2[(\pi/\lambda)(\vec{s}-\vec{s_0})\cdot N_3\vec{a_3}]}{\sin^2[(\pi/\lambda)(\vec{s}-\vec{s_0})\cdot\vec{a_3}]}, \quad \text{(A.13)}$$

in which the Thomson equation was used for I_e (A.5).
This is the scattered intensity from a small crystal and also the definition for the more reknown Laue equations, as constructive interference occurs only if (A.13) is fulfilled in all three dimensions. Conflating the result of the summation over all unit cells in the crystal, i.e., the trigonometric function in eq. (A.13) to the lattice factor (G), the kinematical scattering equation is obtained:

$$I_P = \underbrace{I_e}_{\substack{\text{x-ray / electron interaction}\\ \text{described by Thomson}\\ \text{equation, containing } I_0}} \cdot \underbrace{F^2}_{\substack{\text{structure factor including}\\ \text{atomic distribution}\\ \text{within the unit cell-}\\ \text{gives values of absolute}\\ \text{intensity}}} \cdot \underbrace{G^2}_{\substack{\text{lattice factor, includes}\\ \text{the spatial information}\\ \text{of the unit cell-}\\ \text{gives Bragg peak}\\ \text{distribution in space}}}. \quad \text{(A.14)}$$

A.4 Structure Factor in Diamond Lattice

As Ge and Si have both diamond lattices, the structure factor is calculated to gain insights on the principle existence of Bragg reflections, because, as stated by Eq. (A.13), the intensity vanishes for a vanishing structure factor. Expressing the atomic positions within the unit cell with the fractional coordinates (x_n, y_n, z_n) along the axes $(\vec{a_1}, \vec{a_2}, \vec{a_3})$, the structure factor becomes:

$$F = \sum_n f e^{2\pi i(\mathrm{h}\vec{b_1}+\mathrm{k}\vec{b_2}+\mathrm{l}\vec{b_3})\cdot(x_n\vec{a_1}+y_n\vec{a_2}+z_n\vec{a_3})}.$$

The structure factor of the diamond lattice can be derived as the combination of two fcc lattices, the second shifted by $(\frac{1}{4},\frac{1}{4},\frac{1}{4})$ with respect to the first. The atomic positions in fractional coordinates are: (000), $(0\frac{1}{2}\frac{1}{2})$, $(\frac{1}{2}0\frac{1}{2})$, $(\frac{1}{2}\frac{1}{2}0)$, $(\frac{1}{4}\frac{1}{4}\frac{1}{4})$, $(\frac{3}{4}\frac{3}{4}\frac{1}{4})$, $(\frac{3}{4}\frac{1}{4}\frac{3}{4})$, $(\frac{1}{4}\frac{3}{4}\frac{3}{4})$.

In analogy to the structure factor of the fcc lattice, all mixed hkl planes cause total destructive interference and no intensity is observed. There are two cases left for hkl, i.e., (a) all even or (b) all odd. The structure factor becomes:

$$F = \begin{cases} (a) & \left(4+\left(\cos\frac{3\pi h}{2}+\cos\frac{\pi h}{2}\right)\left(\cos\frac{3\pi k}{2}+\cos\frac{\pi k}{2}\right)\cos\frac{\pi l}{2}\right) \\ (b) & \left(4-i\left(\sin\frac{3\pi h}{2}-\sin\frac{\pi h}{2}\right)\left(\sin\frac{3\pi k}{2}-\sin\frac{\pi k}{2}\right)\sin\frac{\pi l}{2}\right) \end{cases}$$

A sharp look reveals the final structure factor and the corresponding requirements for hkl [32]:

$$F_{diamond} = \begin{cases} 8f & \text{all even, and h+k+l} = 4n \\ 0 & \text{all even, and h+k+l} = 4n+2 \\ (4+4i)f & \text{all odd} \\ 0 & \text{mixed} \end{cases}$$

It has, however, to be noted that in the calculation of the atomic scattering factor the charge density distribution ρ, representing the electron, was assumed to be of spherical symmetry:

$$\rho \rightarrow \rho(r)$$

This approximation is valid for all structures, for which the electrons are located close to the nucleus, as it is the case in strongly ionic bonds. This is not fully true for covalent bonds, as it is the case for Si and Ge, and therefore forbidden peaks might be weakly visible.

B Epitaxial Growth

This part on the background of growth of epitaxial layers is just a very short outline of the extensive principles and theory in the field. Reference to [52] is strongly recommended.

B.1 Thermodynamics

The epitaxial growth of crystals is in general governed, by energetic mechanisms. The equilibrium state is determined by the condition for the global minimum of the free energy of the system. The value that is used to describe the growth of crystals is the chemical potential. It is the derivative of Gibb's free energy, with respect to the particle number n at constant pressure p and temperature T – the conditions of crystal growth in our system. It is defined as the work that has to be done to change the number of particles in the crystal phase by unity

$$\mu = \left(\frac{\partial G}{\partial n}\right)_{p,T}, \tag{B.1}$$

The structure and hence the energy of the epitaxial layer is determined by the interface energy of the adjacent interface of layer and substrate as well as the surface energies of the substrate and the deposit. Furthermore, the strain energies due to misfit, as well as the energies necessary for the nucleation of defects in the deposit contribute. The interplay of these determine the growth modes of the layers on the substrate. The basic considerations of epitaxial growth are derived form crystal growth, meaning the growth of a species on a substrate of the same species. This is the case if, and only if, the two crystals do not differ energetically and geometrically. Epitaxial growth thus takes place if the chemical potentials of the deposit and the substrate differ.

Considering the first monolayer of the deposit, the chemical potential is equal to the work of displacement from its half-crystal position. The work necessary to separate an atom in the first monolayer is determined by, first the bond to the substrate, and second the lateral bond to its neighbor. The lateral bond is not different (idealized) than from the bulk of the layer. Therefore, the difference in the chemical potential must be due to the difference of the bonding to the substrate, which is a consequence of the surface energies of substrate and deposit. For a more accurate treatment, the energies of different crystal planes and packing structures must also be taken into account. As the influence of the substrate on the subsequent monolayer decreases and the surface energies of the bulk crystal planes of the deposit become more influential, the chemical potential is a function of the layer thickness. The general expression for the chemical potential of the first, second, ..., n^{th} monolayer can be written as

$$\mu(n) = \mu_\infty + a^2(\sigma + \sigma_i - \sigma_s) \tag{B.2}$$

with the bulk potential μ_∞, the surface energy of the deposit σ, the interface energy σ_i and the substrate surface energy σ_s. In other words, the chemical potential of each monolayer is the bulk chemical potential

plus the difference of the bonds per atom with the like and unlike crystals. This function of the chemical potential of the layer thickness is the reason for the difference in the well known growth modes of epitaxial films, depicted in Fig. 36:

- $d\mu/dn < 0$: Volmer-Weber growth mode. In this growth mode, the deposit grows in islands, which might or might not coalesce, depending on the kinetics.
- $d\mu/dn > 0$: Frank-van der Merwe growth mode. Here, the deposit grows pseudomorphically layer-by-layer, until the critical thickness is reached. At this thickness the film cracks and misfit dislocations are introduced.
- $d\mu/dn \gtrless 0$: Stranski-Krastanov growth mode. In this mode, first a layer-by-layer mode occurs, but at a certian thickness the layer breaks up and island formation starts. This can only happen if the derivative of the chemical potential changes its sign.

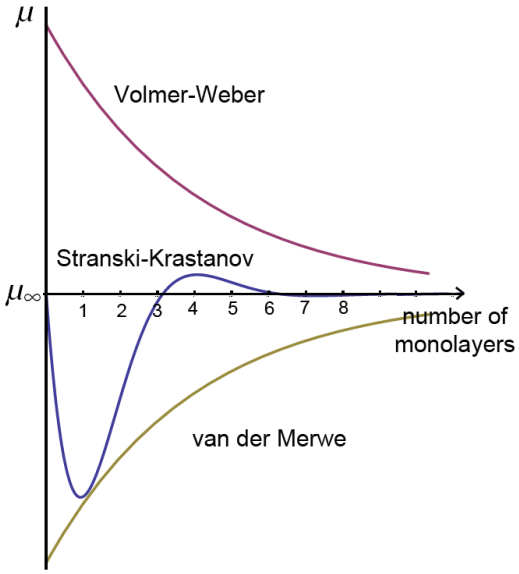

FIG. 36: Scetch of the chemical potential as a function of the number of monolayers in epitaxial growth.

Using the relation of Dupre for misfitting crystals, substituting for the different surface energies, the chemical potential becomes (again as a function of the number of monolayers n)

$$\mu(n) = \mu_\infty + [\phi_a - \phi'_a + \varepsilon_d(n) + \varepsilon_e(n)] \tag{B.3}$$

with the work necessary for separation of one atom from its half-crystal position, with and without the influence of the substrate, ϕ_a and ϕ'_a, respectively, the elastic strain energy $\varepsilon_e(n)$, and the dislocation energy $\varepsilon_d(n)$. This allows for the understanding of the growth modes in a more macroscopic picture, depending on the half-crystal energies.

- $\phi'_a > 0$: The deposit does not grow as good on the surface material as the substrate material itself on the surface. This yields to island formation $\rightarrow$ Volmer-Weber growth.

- $\phi'_a < 0$: The deposit grows even better on the surface than the substrate material itself. This results in layer-by-layer formation → Frank-van der Merwe growth.

- $\phi'_a \gtrless 0$: Initially the deposit grows better than the substrate itself, but with a decreasing influence of the interface, the deposit grows worse. This results in a change from layer-by-layer growth to island formation → Stranski-Krastanov growth.

The latter part of the equation introduces the defect energies, namely the strain and dislocation energies. There are two relaxation mechnism that allow the layer to relax the strain: First, plastic relaxation: For a foreign layer on a substrate below the critical thickness, the strain energy is a function of the thickness. No dislocations are introduced. Above the critical thickness, this is the other way around, and the layer cracks. Second, elastic relaxation: The layer does not grow pseudomorphically and does not crack, but rather continously increases (decreases) its lattice constant. In this macerating of the layer, additional surface is introduced, and thereby additional surface energy attained.
It is noted for completeness, even for the substrate, the chemical potential for the interface region might differ from the substrate value, due to difference of the bond strength of the interface atoms and the substrate. If they are bound more loosely to the substrate the chemical potential becomes higher than for the substrate and vice versa.

B.2 Kinetics

The above derived conditions define the morphology for the equilibrium state. As the state of the system is far from equilibrium, the substrate temperature and deposition rate must be evaluated. Only complete condensation is taken into account, that is to say the atoms of the deposit that impact onto the substrate surface diffuse and start to build 2D islands. The adatom concentration forming on top of the 2D islands is a solution of the diffusion equation in polar coordinates, assuming circular island shape, namely

$$\frac{d^2 n_s}{dr^2} = \frac{1}{r}\frac{dn_s}{dr} + \frac{R}{D_s} \tag{B.4}$$

with the atom arrival rate R, the adatom surface concentration n_s and the surface diffusion rate D_s. This does not take re-evaporation into account. A solution that is found is

$$n_s = n_s^e + \frac{R}{4D_s}(\rho_1^2 - r_1^2) - (\Delta n_s + \frac{R}{4D_s}(\rho_1^2 - r_1^2)) \cdot A \tag{B.5}$$

with the additional concentration differences Δn_s of monolayers oone and two, the island sizes $\rho_{1,2}$, and a size dependent variable A. Supposing now that $\mu(1) > \mu(2)$, namely that $d\mu/dn < 0$, then the deposit of monolayer 2 on top is supersaturated with respect to the bulk crstal. This favors nucleation on top of the islands. If then, additionally, the equilibrium surface concentration with the island edges is higher for the first monolayer than for the second, transport from the edges of the lower monolayer to the edge of the upper will occur. In this case, the upper layer grows, while the lower shrinks, until an island with

double height has formed.

Therefore, if the chemical potential is a decreasing function of the layer thickness, island growth will occur for high enough temperatures at that the inter surface diffusion is activated. Nevertheless, if the temperature is low enough, so that no transport from the lower edges to the upper edges is taking place, layer by layer growth will start before significant growth on top of the first monolayers occurs. The layer-like growth takes place due to the kinetics of the atoms in the evaporation beam and not the thermodynamic trend to the equilibrium. Those films are metastable: They will break up as soon as the transition temperature is reached. A true layer by layer growth only takes place if the chemical potential of the second monolayer is higher than the chemical potential of the first monolayer.

If the epitaxial growth proceeds, crystal growth of the deposit is more important than the conditions at the interface. At a temperature at which no high energy facets are activated, the system will favour the formation of its facets with the lowest surface energy.

C Scientific Publications

Peer Reviewed Scientific Publications

1. A. Giussani, O. Seifarth, P. Rodenbach, H.-J. Müssig, P. Zaumseil, T. Weisemöller, C. Deiter, J. Wollschläger, P. Storck, and T. Schroeder.
   The influence of lattice oxygen on the initial growth behavior of heteroepitaxial Ge layers on single crystalline PrO_2(111)/Si(111) support systems
   Journal of Applied Physics **103**, 084110 (2008).

2. A. Giussani, P. Rodenbach, P. Zaumseil, J. Dabrovski, R. Kurps, H.-J. Müssig, P. Storck, and T. Schroeder.
   Atomically smooth and single crystalline Ge(111) / heterostructures: structural and chemical composition study
   Applied Physics Letters (submitted).

3. P. Zaumseil, A. Giussani, P. Rodenbach, and T. Schroeder.
   X-ray characterization of epi-Ge / cub-Pr_2O_3(111) / Si(111) layer stacks by pole figures and reciprocal space mapping
   Physics Status Solidi C (submitted).

4. P. Rodenbach, A. Giussani, P. Zaumseil and T. Schroeder.
   Defect engineering in Ge (111) heterostructures: a threading behaviour and treatment study.
   Applied Physics Letters (in preparation).

Own Talks:

1. P. Rodenbach, A. Giussani, J.I. Pascual, D. Geiger, H. Lichte, P. Storck, T. Schroeder.
   100% epi-Ge layers on engineered oxide heterostructures on Si
   72^{nd} Annual Meeting of the Deutsche Physikalische Gesellschaft, Berlin 2008.

Conference contributions

1. A. Giussani, Ch. Wenger, O. Seifarth, A. Wilke, P. Rodenbach, P. Storck, J.Dabrowski, P. Zaumseil, H.-J. Müssig, M. Lukosius, and T. Schroeder
   Engineered Si Wafers: SOI & GOI via Oxide Heterostructures
   Workshop on Dielectrics in Microelectronics 2008, Bad Sarow (Germany).

2. A. Giussani, O. Seifarth, P. Rodenbach, P. Zaumseil, G. Weidner, H.-J. Müssig, P. Storck, T. Schroeder.
   Heteroepitaxial Integration of Single Crystalline Ge(111) Layers on Si(111) via PrO_2 (111) Heterostructures
   Electrochemical Society Transactions, Honolulu (USA). Vol **13**. "SiGe, Ge, and related Compounds 3" October 2008.

Danksagungen

Ich bedanke mich bei all denen, die dazu beigetragen haben, dass mir das Studium, welches in dieser Arbeit seinen Abschluss findet, möglich war.
Besonderer Dank gilt Prof. J.I. Pascual an der Freien Universität Berlin, der mir die Ausführung dieser externen Arbeit über seine Arbeitsgruppe ermöglichte sowie die Betreuung meiner Arbeit übernommen hat. Gleichermassen bedanke ich mich bei Dr. Thomas Schröder, der die intensive direkte Betreuung meiner Arbeit am IHP in Frankfurt übernommen hat, und besonders neben dem wissenschaftlichen Anspruch an meiner Zuarbeit auch stets sehr an einer humanistischen Allgemeinbildung in Bezug auf die Übersicht über die aktuelle Forschungslandschaft interessiert war und der meine durchaus nicht übliche Beteiligung an den genannten Veröffentlichungen vorangetrieben hat. Besonders hat mich das anscheinend unerschöpfliche Fachwissen, untermauert durch die jederzeit aus dem Schrank 'zauberbaren' Veröffentlichungen, nachhaltig beeindruckt.
Ich bedanke mich bei allen Kollegen der Materialforschung am IHP, die mir mit Rat und Tat zur Seite gestanden haben, insbesondere bei der Einarbeitung in die laufende Projektarbeit und die Bedienung der Messgeräte. Mit A. Giussani, Dr. T. Schroeder, Dr. P. Zaumseil und H. Thieme sind hier nur diejenigen genannt, die am meisten Zeit für mich aufgewendet haben. Ebenso bedanke ich mich bei meinen Komilitonen, die mich während meines Studium begleitet haben, für die unzähligen Diskussionen und gemeinsam verbrachten Lehrnsitzungen, insbesondere auch für die kritische Korrektur dieser Arbeit. Ohne diese Zusammenarbeit und gegenseitige Unterstützung hätte ich das Studium sicherlich nicht in der jetzigen Art und Weise beendet.

Meiner Familie und meinen Freunden danke ich für die bedingungslose Unterstützung und Freundschaft.

Danke euch allen.

References

[1] Eugene A. Fitzgerald, Mat. Sci. Eng., B **124-125**, 8 (2005).

[2] Howard Huff, J. Electrochem. Soc. **149** (5), 35 (2002).

[3] Gordon E Moore, Electronics, **38** (8), (1965).

[4] for further information see *www.intel.com*

[5] Rainer Waser, *Nanoelectronics and Information Technology* Wiley-VCH, Weinheim, Second Edition, 2005

[6] Yoshiki Kamata, Mater. Today **11**, 30 (2008)

[7] S.B. Samavedam, M.T. Currie, T.A. Langdo, E.A. Fitzgerald, Appl. Phys. Lett. **73**, 2125 (1998).

[8] Takeshi Akatsu, Chrystel Deguet, Loic Sanchez, Frederic Allibert, Denis Rouchon, Thomas Signamarcheix, Claire Richtarch, Alice Boussagol, Virginie Loup, Frederic Mazen, Mater. Sci. Semicond. Proess. **9**, 444 (2006).

[9] M. Oehme, J. Werner, E.Kasper, S. Klinger, M. Berroth, Appl. Phys. Lett. **91**, 051108 (2007).

[10] G.F.X. Strobl, R. Dietrich, J. Hilgarth, R. Kern, W. Koestler, G. LaRoche, M. Meusel, D. Poeck, K.D. Rasch, W. Zimmermann, *Evolution of fully European Triple GaAs Solar Cell* Proc. of "Seventh European Space Power Conference", 2005.

[11] A.S. Cooper, Acta Crystallogr. **15**, 578 (1962)

[12] Ben Dpuydt, Antoon Theuwis, Igor Romandic, *Germanium based Technologies - From Materials to Devices* Elsevier Science, Kidlington, UK, First edition, 2007.

[13] for further information see *www.umicore.com*

[14] J. Derluyn, K. Dessein, G. Flamand, Y. Mols, J. Poortmans, G. Borghs, I. Moerman, J. Cryst. Growth **310**, 6 (2003)

[15] Michel Bruel, *Process for the Manufacture of thin films of semiconductor material*. U.S. patent 5714395

[16] Clarence J. Tracy, Peter Fejes, N. David Theodore, Paul Maniar, Eric Johnson, Albert J. Lamm, Anthony M. Paler, Igor J. Malik and Phillip Ong, J. Electron. Mater. **33**, 886 (2004).

[17] J.D. Cressler, *The Silicon Heterostructure Handbook: Materials, Fabrication, Devices, Circuits, and Applications of SiGe and Si Strained-Layer Epitaxy,* CRC Press, New York, 2005.

[18] for further information see *www.ihp-microelectronics.com/19.0.html*

[19] T. Schroeder, P. Zaumseil, G. Weidner, C. Wenger, J. Dabrowski, H.-J. Müssig, J. Appl. Phys. **99**, 014101 (2006).

[20] T. Schroeder, I. Costina, A. Giussani, G. Weidner, O. Seifarth, Ch. Wenger, P. Zaumseil, C. Mocuta, T.H. Metzger, J. Appl. Phys. **102**, 034107 (2007).

[21] T. Weisemoeller, C. Deiter, F. Bertram, S. Gevers, A. Giussani, P. Zaumseil, T. Schroeder, J. Wollschläger, Appl. Phys. Lett. **93**, 032905 (2008).

[22] A. Giussani, O. Seifarth, P. Rodenbach, H.-J. Müssig, P. Zaumseil, T. Weisemoeller, C. Deiter, J. Wollschlaeger, P. Storck, T. Schroeder, J. Appl. Phys. **103**, 084110 (2008).

[23] G.W. Trucks, K. Raghavachari, G.S. Higasgi, Y.J. Chabal, Phys. Rev. Lett. **54**, 504 (1990).

[24] W. Kern and D. A. Puotinen, RCA Rev. **31**, 187 (1970).

[25] G.S. Higashi, Y. Chabal, G. Trucks, K. Raghavachari, Appl. Phys. Lett. **56**, 656 (1990).

[26] M. Henzler, W. Göpel, *Oberflächenphysik des Festkörpers*, Teubner Studienbücher Physik, Stuttgart, 1991.

[27] J.P. Liu, P. Zaumseil, E. Bugiel, H.J. Osten, Appl. Phys. Lett. **79**, 671 (2001).

[28] T. Schroeder, T. Lee, L. Libralesso, I. Joumard, J. Zegenhagen, P. Zaumseil, Ch. Wenger, G. Lupina, G. Lippert, J. Dabrowski, H. Müssig, J. Appl. Phys. **97**, 075906 (2005).

[29] R.T. Tung, J. Bean, J. Gibson, J. Poate, D. Jacobson, Appl. Phys. Lett. **40**, 684 (1982).

[30] Thomas Schroeder, *Towards high quality epi-SiGe/high-k dielectrics/Si(111) heterostructures: Interface engineering by amorphous dielectrics and lattice matching by mixed epitaxial buffer oxides*. 5. International Conference on Silicon Epitaxy and Heterostructures, Marsaille 2007.

[31] H. Tabata, E. Ishii, H. Okuda, J. Chryst. Growth **52** 956 (1981).

[32] M. Birkholz, *Thin Film Analysis by X-Ray Scattering*, Wiley-VCH Verlag, Weinheim, 2006.

[33] B.E.Warren, *X-Ray Diffraction*. Dover Publications Inc., New York, Reprint, 1990.

[34] H. Kiessig, Anna. Phys. **402**, 715 (1931).

[35] Peter Zaumseil, *RCRefSim*, (Rocking curve and reflectivity simulation), Frankfurt(Oder), 2005. zaumseil@ihp-microelectronics.com

[36] J. Als-Nielsen, Des McMorrow, *Elements of Modern X-ray Physics*, John Wiley & Sons, Ltd., New York, 2001.

[37] I. Hernandez-Calderon, H. Höchst, Phys. Rev. B **27**, 4961 (1983).

[38] W. Braun, *Applied RHEED*, Springer Verlag, Berlin, 1999.

[39] J.W. Seo, Ch. Dieker, A. Tapponnier, Ch. Marchiori, M. Sousa, J.-P. Locquet, J. Fompeyrine, A. Ispas, C. Rossel, Y. Panayiotatos, Sotiropoulos, A. Dimoulas, Microelectron. Eng. **84**, 2328 (2007).

[40] S. Ohmi, T. Kazuo, S. Furukawa, Jpn. J. Appl. Phys. **33**, 1121 (1994).

[41] H. J. W. Zandvliet, A. Van Silfhout, Surf. Sci. **195**, 138 (1988).

[42] F. Bechstedt, A. Stekolnikov, J. Furthmüller, P. Käckell, Phys. Rev. Lett. **87**, 016103 (2001).

[43] P. Zaumseil, J. Phys. D: Appl. Phys. **41**, 135308 (2008).

[44] TEM images from personal reference,
D. Geiger, H. Lichte, Technical University Dresden, Zellscher Weg 16, 01062 Dresden, Germany.

[45] R. Drosd, J. Washburn, J. Appl. Phys. **53**, 387 (1982).

[46] P.Zaumseil, A. Giussani, P. Rodenbach, T. Schroeder, Phys. Status Solidi submitted, (2008).

[47] U. Pietsch, V. Holy, T. Baumbach, *High Resolution X-Ray Scattering: From Thin Films to Lateral Nanostructures*. Springer-Verlag, New York, 2004.

[48] K. Nordlund, U. Beck, T. Metzger, J. Patel, Appl. Phys. Lett. **76**, 846 (2000).

[49] Y. Morishita, Y. Nomura, S. Goto, Y. Katayama, Appl. Phys. Lett. **67**, 2500 (1995).

[50] B.D. Culity, S.R. Stock, *Elements of X-Ray Diffraction*, Addison-Weseley Publishing Company, Inc. Reading, Massachusetts, 1978.

[51] Spiess, Schwarzer, Behnken, Teichert, *Moderne Röntgenbeugung*, Teubner Verlag, Wiesbaden, 2005.

[52] I. Markov, *Crystal Growth for Beginners*, World Scientific Publishing Co. Pte. Ltd., London, 1995.

[53] B.G. Hyde, D.J.M. Devan, L. Eyring, Philos. T. Roy. Soc. A **259**, 583 (1965)

[54] T. Schroeder, P. Zaumseil, O. Seifarth, A. Giussani, H.-J. Müessig, P. Storck, D. Geiger, H. Lichte, and J. Dabrowski, New J. Phys., accepted.

[55] V. De Renzi, R. Biagi, U. del Pennino, Surf. Sci. **497**, 247 (2002).

[56] B.L. Henke, E.M. Gullikson, and J.C. Davis, Atomic Data and Nuclear Data Tables **54, No.2**, 181-342 (1993).

[57] C. Ball, J.H. van der Merwe, Phys. Stat. Sol. **38**, 335 (1970).

[58] F. Ernst, P. Pirouz, J. Appl. Phys. **64**, 4226 (1988).